THE ASTROPHYSICAL JOURNAL, 439:939–956, 1995 February 1

INFRARED ZEEMAN ANALYSIS OF ϵ ERIDANI

JEFF A. VALENTI
Astronomy Department, University of California, Berkeley, CA 94720
GEOFFREY W. MARCY[1]
Physics and Astronomy Department, San Francisco State University, San Francisco, CA 94132
AND
GIBOR BASRI
Astronomy Department, University of California, Berkeley, CA 94720
Received 1994 May 26; accepted 1994 August 4

ABSTRACT

We analyze high-resolution infrared FTS spectra near 1.6 μm to obtain the most accurate measurement to date of the magnetic field on a typical active star. A total of 16 infrared Fe I lines are analyzed, including the $g_{\rm eff} = 3$ line at 1.56485 μm. We find that 8.8% of the deep photosphere of the active star ϵ Eridani (K2 V) is covered with a 1.44 kG magnetic field. This corresponds to an absolute magnetic flux of $|\boldsymbol{B}|f = 0.13$ kG, which is about half the value found in all recent optical studies but agrees with the one existing infrared upper limit. We discuss possible explanations for this discrepancy in terms of models with different atmospheres for the quiet and magnetic components.

We carefully assess the impact of random noise on our derived magnetic parameters and find that the quantity $|\boldsymbol{B}|f^{0.8}$ is most accurately known, with a formal uncertainty of 0.1%. The 1 σ confidence interval *along* this curve ranges between $(|\boldsymbol{B}|, f) = (1.31$ kG, 10.0%) and (1.60 kG, 7.8%). We also study various sources of systematic errors, and find a 35% uncertainty in f, primarily because the structure of stellar flux tubes is poorly known, but also because of uncertainty in log g. Systematic errors in $|\boldsymbol{B}|$ are smaller (less than 15%) because the σ components of the 1.56485 μm line are resolved. We place low upper limits on the surface magnetic flux on two inactive stars, 40 Eri (K1 V) and σ Dra (K0 V), reinforcing the significance of our magnetic field detection for ϵ Eri.

As a byproduct of the Zeeman analysis, we have derived accurate effective temperatures, iron abundances, and macroturbulences for all three stars. In addition, we have determined oscillator strengths (most previously unmeasured) for 21 Fe I transitions near 1.6 μm by matching models to the observed solar spectrum.

Subject headings: line: profiles — stars: activity — stars: fundamental parameters — stars: individual (ϵ Eridani) — stars: magnetic fields

1. INTRODUCTION

Magnetic fields play a fundamental role in the physics of late-type stellar atmospheres, yet our understanding of the underlying hydromagnetic processes is limited, in part because we lack adequate data to test our theories. Magnetic fields control the formation and evolution of flares, spots, and active regions, and they are primarily responsible for transporting and depositing energy into the chromosphere and corona. Heating of the upper atmosphere leads to solar-type mass loss and controls angular momentum evolution. A hydrodynamic dynamo, driven by the interaction of differential rotation and convection, generates these magnetic fields. A wealth of solar data and theories is available to explain these phenomena, but it is difficult to assess these results in the broader stellar context. To overcome this problem, accurate magnetic parameters are needed for a sample of cool stars that span the observed range of activity and dynamo parameters.

Magnetic fields have been detected on late-type stars (Robinson 1980; Saar 1988; Mathys & Solanki 1989; Marcy & Basri 1989) by identifying excess line broadening in Zeeman sensitive transitions, i.e., those with high effective Landé-g factors ($g_{\rm eff}$). Stellar Zeeman analysis programs have become increasingly sophisticated since Robinson's pioneering work. The state of the art currently involves using a polarization-sensitive radiative transfer code to simultaneously model many line profiles, preferably in the infrared where the Zeeman effect is more pronounced.

Spectral lines are composed of linearly polarized π components and elliptically polarized σ components. In the presence of a magnetic field the energies of the initial and final states change by an amount dependent on m_J, thereby changing the wavelength of photons absorbed (or emitted) during transitions between these two states. The components shift in wavelength by an amount

$$\Delta\lambda = 0.00467 g \left(\frac{\lambda}{1\ \mu\text{m}}\right)^2 \left(\frac{|\boldsymbol{B}|}{1\ \text{kG}}\right) \text{nm}\ , \qquad (1)$$

where g is the Landé factor of each component, λ is the unperturbed wavelength of the transition, and $|\boldsymbol{B}|$ is the strength of the magnetic field in the line formation region.

There are many advantages in using near infrared lines to study stellar magnetic fields. Zeeman splitting of σ components is proportional to wavelength squared, whereas intrinsic line width is simply proportional to wavelength. In particular, the splitting of the σ components in the Fe I line at 1.56485 μm is 2–3 times the splitting in even the most Zeeman-sensitive optical lines (e.g., 617.33 and 846.84 nm). This line has been

[1] Visiting Astronomer, Astronomy Department, University of California, Berkeley, CA 94720.

used to measure magnetic fields in solar plage (Rüedi et al. 1992), network (Muglach & Solanki 1992), and spots (Solanki et al. 1992a). Continuous opacity is lowest near 1.6 μm, so lines near this wavelength form deepest in the atmosphere where equipartition models predict higher magnetic fields. The line density is lower than in the optical, so blends are less of a problem in the infrared. The Ti I multiplet near 2.2 μm also contains a number of useful Zeeman diagnostics, including the $g_{\rm eff} = 2.5$ line at an air wavelength of 2.23106 μm. Saar & Linsky (1985) used these lines to measure 3 kG fields on the very active M star AD Leo.

Zeeman split σ components can actually be resolved in the near infrared. In particular, the Fe I line at 1.56485 μm is a Zeeman triplet in which the σ components have $g = 3$. At field strengths of 1.5 kG, typical of late-type, main-sequence stars (Saar 1990), the σ components are separated by $2\Delta\lambda = 0.1$ nm, which is twice the typical FWHM of this line in slowly rotating K stars. Even in the most Zeeman sensitive of optical lines (e.g., 617.33 and 846.84 nm), separation of σ components is at best only comparable to the line width, due to the wavelength dependence of the Zeeman effect.

Although the σ components of the 1.56485 μm line are resolved in stellar flux tubes, detecting these σ components in actual stellar spectra is still complicated. Magnetically perturbed profiles from flux tubes are diluted by flux contributions from surface regions with little or no magnetic field. Since flux tubes cover no more than 50% and typically less than 10% of an active star, this dilution can be substantial. The σ components appear as inflection points in the line wings, rather than as distinct local minima in the spectrum. Nonetheless, these inflection points (and the extended wings they represent) are much more sensitive diagnostics of stellar magnetic fields than the broadening of line cores seen in the optical.

Optical studies have been plagued by ambiguities in field strength, $|\boldsymbol{B}|$, and surface covering fraction, f, of flux tubes. When σ components are unresolved (as they are in the optical), it is possible to trade $|\boldsymbol{B}|$ for f, though the exact exchange rate is uncertain. The problem is especially acute when only a few lines are included in the analysis, making it difficult to distinguish between Zeeman and other nonmagnetic broadening mechanisms. Because of this ambiguity, values of $|\boldsymbol{B}|f$ or $|\boldsymbol{B}|f^{0.5}$ are usually considered much more reliable than the values of $|\boldsymbol{B}|$ and f separately (Saar 1990). This ambiguity is lifted for the 1.56485 μm line, which has resolved σ components.

There are a dozen lines near 1.56 μm that have Landé-g factors of about 1.5. Because of their longer wavelengths, these lines all have Zeeman sensitivities comparable to or better than the best optical diagnostics! The σ components of these lines are still unresolved, however, so a multiline profile analysis is required to extract the Zeeman information. By carefully modelling many spectral lines, thermal, collisional, turbulent, and rotational broadening can all be measured (e.g., Drake & Smith 1993, hereafter DS) and distinguished from magnetic broadening. Of great importance in this procedure are the few lines with very low Landé-g factors, which help define the behavior of the unperturbed atmosphere. Finally, inactive stars may be used to evaluate the accuracy of the stellar models used in multiline Zeeman analyses.

In § 2 we present the optical and infrared spectra that we use in this study. In § 3 we use the solar spectrum to deduce atomic parameters (a collisional broadening parameter and oscillator strengths) for Fe I lines in our spectra. In § 4 we describe the structure of stellar magnetic fields. In § 5 we describe the procedure by which we measure stellar magnetic fields. Section 6 gives the results of our Zeeman analysis, which are discussed in § 7.

2. OBSERVATIONS

2.1. *Procedure*

We obtained infrared spectra of ϵ Eri, 40 Eri, σ Dra, and α CMa (Sirius) using the Fourier transform spectrometer (FTS; Hall et al. 1979), fed by the 4 m Mayall telescope at Kitt Peak National Observatory. A symmetric scan distance of 19.54 cm was selected, yielding an instrumental FWHM of 0.0152 nm (0.0619 cm^{-1}) and a resolution of 1.03×10^5. The spectra were never apodized, so the appropriate instrumental profile is a sinc function.

For each observation, Table 1 lists the UT date and time at the beginning of each exposure (cols. [2] and [3]), the exposure duration in hours (col. [4]), and the time-averaged airmass (col. [5]). Above an airmass of 2, exposures were limited to a duration of less than 45 minutes, thereby limiting large changes in airmass over the course of the observation, which would hamper the removal of telluric features. The sky was clear during the first two nights. On the third night, however, variable cirrus caused about 1 mag of extinction. As discussed below, the cirrus had little effect on the telluric correction because the prominent telluric features in our bandpass are due to CO_2, rather than water vapor.

Our observing procedure consisted of scanning the full interference pattern in both the forward and reverse directions with the star in one aperture, and then repeating the process with the star switched to the other aperture. Each such group of

TABLE 1

INFRARED FTS OBSERVATIONS

Star (1)	UT Date (1992) (2)	Start Time (h:m:s) (3)	Duration (hr) (4)	Airmass (5)
ϵ Eri[a]	Nov 14	3:31:28	0.68	2.44
	Nov 14	4:14:28	3.04	1.56
	Nov 15	3:25:59	0.69	2.47
	Nov 15	4:09:44	2.71	1.59
	Nov 16	4:55:40	1.47	1.50
40 Eri[b].....	Nov 14	7:27:14	2.69	1.36
	Nov 14	10:13:37	1.36	1.84
	Nov 14	11:38:16	0.69	2.72
	Nov 15	6:55:19	3.38	1.37
	Nov 16	6:27:16	1.36	1.34
σ Dra[c]	Nov 14	0:34:03	2.73	1.38
	Nov 15	0:53:43	1.05	1.34
	Nov 15	1:58:56	1.35	1.46
	Nov 16	0:45:10	0.34	1.31
	Nov 16	1:07:59	1.74	1.40
	Nov 16	2:55:03	1.37	1.61
α CMa[d].....	Nov 14	12:32:42	0.17	1.86
	Nov 14	13:00:13	0.35	2.08
	Nov 14	13:37:30	0.35	2.56
	Nov 14	13:59:49	0.35	3.04
	Nov 15	10:22:03	0.35	1.51
	Nov 16	10:13:16	0.35	1.52
	Nov 16	12:00:19	0.35	1.77

[a] ϵ Eri = HD 22049 = HR 1084.
[b] 40 Eri = HD 26965 = HR 1325.
[c] σ Dra = HD 185144 = HR 7462.
[d] α CMa = HD 48915 = HR 2491 = Sirius.

four scans required 19.21 minutes. Balancing the number of scans in each direction and aperture reduces errors that arise due to differences along the various optical paths and differences in the two detectors (C and D). Longer observation consisted of integral multiples of this basic time plus overhead and occasionally a small amount of time during which the observation was temporarily halted. Each star was observed for a total of about 9 hr.

Thermal noise outside our bandpass was blocked with a pair of filters purchased from Barr Associates (one for each aperture). At an operating temperature of 77 K, the central wavelength passed by these filters is 1.5665 μm (6381.9 cm^{-1}) with a peak transmission of 73%. The FWHM is 45 nm (180 cm^{-1}), which is 2.8% of the central wavelength. The peak of the filter is rather flattened, so that the full width at 90% of the peak transmission (i.e., at 66% transmission) is 28 nm (110 cm^{-1}).

2.2. *Telluric Absorption*

Our spectra contain two prominent telluric CO_2 bands (Park et al. 1987) redward of 1.567 μm. About 25 lines are visible in each of these CO_2 bands, with the cores of the strongest lines approaching zero intensity, making this part of the spectrum unsuitable for high-precision spectroscopic analysis. The presence of such strong telluric bands in our spectra also induces a Fourier ringing in the form of a ripple with an amplitude of about 2% of the continuum intensity. The ripple has a period of 1.2 nm (5 cm^{-1}), which matches the mean spacing between adjacent CO_2 lines. The amplitude of the ripple varies with depth of the CO_2 bands, which in turn scales with the airmass during the observation. Our procedure for removing telluric absorption features (see below) also removes the CO_2 induced ripple.

Where the spectra are not contaminated by these two CO_2 bands, they are remarkably free of any telluric absorption. By examining our raw spectra of Sirius and also very high quality FTS spectra of Earth's atmosphere (Livingston & Wallace 1991), we find that there are no telluric features deeper than 2% in the wavelength range 1.552 to 1.569 μm. In fact the few detectable telluric features in this range are almost all considerably weaker than 2%. We restrict our multiline Zeeman analysis to wavelengths between 1.553 and 1.569 μm, which are free of even moderate telluric absorption.

In order to model and correct for weak telluric absorption (and also the ripple discussed above), we observed Sirius at airmasses between 1.5 and 3.0 (see Table 1). We constructed a model of residual intensity versus airmass at each wavelength in the spectra of Sirius. This model was then scaled to the mean airmass for each observation (see Table 1) and used to remove both the telluric absorption features and the ripple. There are a couple of weak water vapor lines in our spectrum that may not have been properly removed, due to variations in the humidity during our observations, but these lines do not in any way affect the results of our Zeeman analysis. All other telluric features are undetectable in the corrected spectra.

2.3. *FTS IR Spectra*

After correcting each observation for telluric absorption and ripple, we aligned and added spectra of each star. Observations were trimmed to the wavelength range 1.552–1.569 μm, cross-correlated with a raw sum, and then added. Observations were weighted according to their exposure time in the raw sum, and according to their S/N in the final sum. The continua were normalized by dividing each summed spectrum by a fourth-order polynomial fit to local medians computed in 20 bins across the spectrum. Only the highest 15% of the points were used in each bin, so as to exclude spectral lines. Measured noise levels in the final summed spectra are 0.47% for ϵ Eri, 0.63% for 40 Eri, and 1.12% for σ Dra. All percentages are measured with respect to the peak continuum flux in each spectrum. These noise estimates are standard deviations of the baseline in our summed spectra, measured at wavelengths outside our filter bandpass (1.8 to 2.0 μm). Since we are using an FTS, noise is independent of wavelength. Analysis of a much narrower continuum window between 1.5546 and 1.5548 μm gives a much less accurate, but consistent, noise estimate.

Figure 1 shows our infrared FTS spectra of ϵ Eri, 40 Eri, and σ Dra. The continuum has been normalized, and then offset by +0.3 for 40 Eri and +0.6 for σ Dra. Only the trimmed spectra, used in the Zeeman analysis, are presented. The longer wavelength region containing two strong CO_2 bands is not shown. There is 0.2 nm of overlap between successive panels. Vertical arrows indicate the wavelengths of 21 Fe I lines, which we used to model the Sun and to determine atomic parameters. Only the 16 spectral lines indicated by solid arrows were used in the Zeeman analysis, however. The magnetically sensitive $g_{eff} = 3$ line at 1.56485 μm is labeled at the left edge of the lower panel.

In constructing our line sample, we considered every Fe I transition with a line visible in our trimmed spectra. Some of the lines are quite weak and therefore provide relatively weak constraints in our Zeeman analysis. Other lines are partially blended, so that only a portion of the profile can be used in the analysis. Five of these heavily blended profiles are excluded from the stellar Zeeman analysis. The Fe I line at 1.56112 μm was excluded from our analysis because it shows anomalous Stokes V behavior (Muglsch & Solanki 1992). Similarly, the Fe I lines at 1.55915 and 1.55678 μm were excluded because we had difficulty matching these lines in the solar spectrum (described below), perhaps due to blends buried in the profiles. None of the remaining lines visible in the spectrum are due to identified transitions of Fe I.

2.4. Ca II H *and* K *Diagnostics*

In addition to the infrared spectra, we also obtained simultaneous optical spectra of ϵ Eri and 40 Eri. These spectra were obtained with the Hamilton echelle spectrometer (Vogt 1987) at Lick Observatory, fed by the 3 m Shane telescope. The cross-dispersed spectrometer has a spectral resolution of 45,000 and covers the entire optical spectrum, including the important activity diagnostics Ca II H and K. Table 2 summarizes the UT date and time (cols. [2] and [3]), duration (col.

TABLE 2

OPTICAL OBSERVATIONS

Star (1)	UT Date (1992) (2)	Start Time (hh:mm:ss) (3)	Duration (s) (4)	Airmass (5)
ϵ Eri	Nov 14	7:54:27	125	1.46
	Nov 14	8:02:46	130	1.46
	Nov 14	8:10:24	135	1.46
	Nov 14	8:18:13	130	1.46
	Nov 16	7:28:01	150	1.47
	Nov 16	7:37:23	50	1.47
40 Eri.....	Nov 14	8:25:59	250	1.42
	Nov 14	8:36:29	250	1.41
	Nov 14	8:46:13	260	1.41

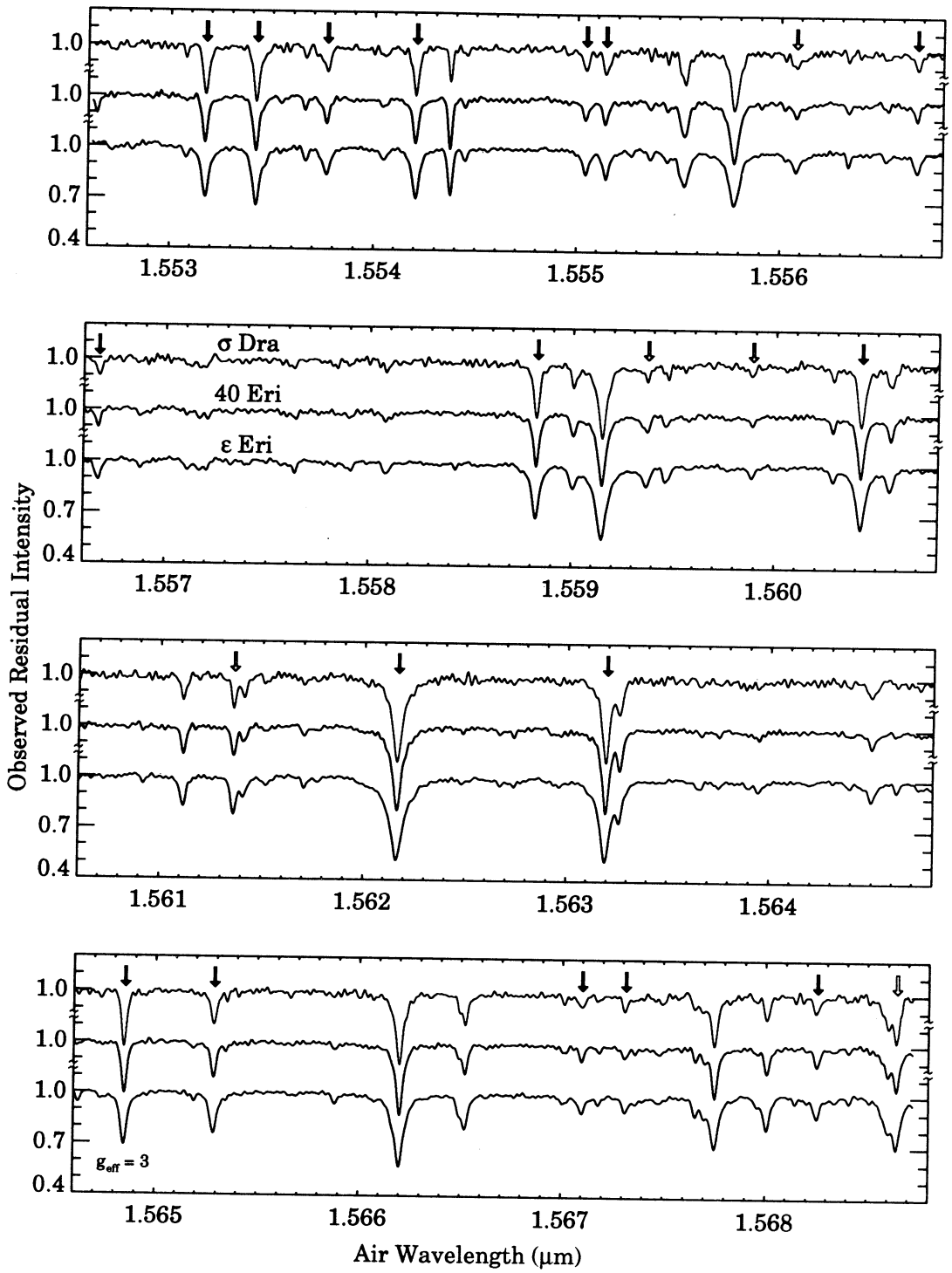

FIG. 1.—Residual intensity spectra ($R = 1.03 \times 10^5$) of ϵ Eri, 40 Eri, and σ Dra, obtained with the infrared FTS at KPNO. All spectra have the same vertical scale, but 40 Eri and σ Dra have been displaced vertically by 0.3 and 0.6 continuum units respectively. Empirical log gf values were determined for the Fe I lines indicated by arrows (see Table 3). Filled arrows indicate lines used in the Zeeman analysis. The magnetically sensitive $g_{eff} = 3$ line is identified at the left edge of the bottom panel.

[4]), and mean airmass (col. [5]) of each exposure. The spectra were extracted from the raw images using our echelle reduction package written in IDL. Consecutive exposures of each star were added prior to spectral extraction.

Figure 2 shows Ca II H spectra of ϵ Eri (*solid profile*) and 40 Eri (*dotted profile*). These data were obtained during the first night of infrared FTS observations (see Tables 1 and 2). We also have a second optical spectrum of ϵ Eri (not shown in Fig. 2), obtained on the last night of the infrared observations. The spectra have been smoothed with a 5 pixel boxcar function for presentation purposes. The effective resolution in the plots is 24,000 (FWHM = 0.0165 nm), but we used the unsmoothed

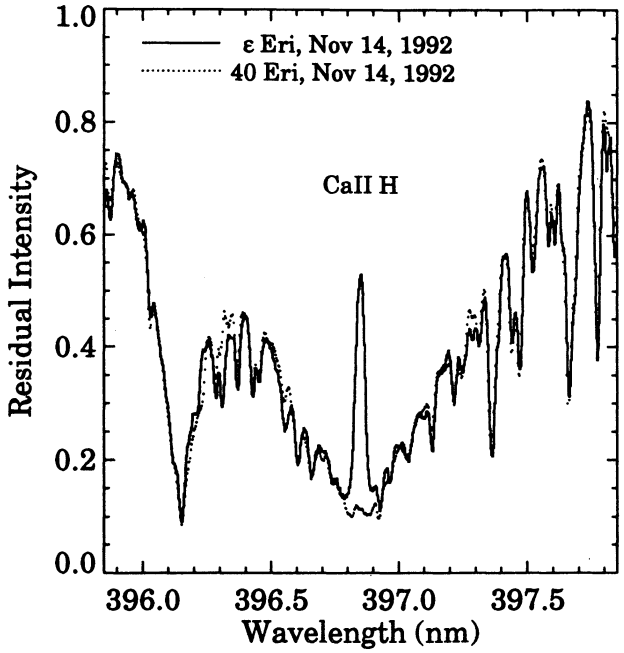

FIG. 2.—Hamilton echelle spectra of the Ca II H lines of ϵ Eri and 40 Eri, obtained during the first night of the IR FTS observations. The spectra have been smoothed with a boxcar filter, yielding an effective resolution (FWHM/λ) of 24,000.

spectra in the emission analysis described below. A global scattered light correction (10%–15% of the continuum) was applied to each spectrum to force agreement throughout the wings of the Ca II H profiles.

We present the Ca II H line, rather than the more traditional K line, because the noise in the K profile is significantly worse, due to falling CCD sensitivity in the blue and less favorable placement relative to the blaze function. The Hϵ line of H I can contaminate H line measurements, especially in hotter stars and at lower resolution, but it is so weak in our spectra that it can barely be discerned.

The emission reversal in ϵ Eri is seen more clearly in Figure 3, which is an expanded view of the central region of Figure 2. It is clear that ϵ Eri was indeed chromospherically (and therefore magnetically) active during our infrared observations. Moreover, the level of activity is nearly the same in the two observations of ϵ Eri, suggesting that the activity level was fairly constant. Note that our infrared observations of ϵ Eri spanned 2.06 days, which constitutes 18% of the 11.3 day observed rotation period (Noyes et al. 1984). Thus, over the course of our infrared observations, we sampled 68% of the surface of ϵ Eri.

To place the activity level of ϵ Eri in some context, we calculated r_H, the average residual intensity in the core of the Ca II H line that would be measured with the HKP-2 spectrometer described by Duncan et al. (1991). We were unable to directly compare the line core and continuum fluxes because the response of the echelle spectrometer is a strong function of wavelength. Instead, we adopted the continuum level of the Kurucz et al. (1984) solar atlas by matching the wings of our Ca II K profiles to the solar profile. A similar procedure was used by Duncan et al. (1991) to convert the continuum bandpasses of the actual HKP-2 spectrometer to true continuum levels. We then multiplied the observed spectra with the normalized bandpass curve for the HKP spectrometer and integrated over the line profile. Using our values of r_K, we calculated S, the standard instrumental index of Ca II H and K line flux reported by the HKP-2 spectrometer. We assumed that the mean residual intensity over both lines, r_{HK}, was equal to our value of r_K. Then, using equation (5) of Duncan et al. (1991),

$$S = 1.54 r_{HK} + 0.040 , \quad (2)$$

we computed S for each of our three optical observations. We determined values of 0.499 (November 14) and 0.485 (November 16) for ϵ Eri and 0.231 for 40 Eri (November 14).

We tested the accuracy of our S values, determined from high-resolution spectra, by comparing them with actual S values from the HKP-2 spectrometer. By a fortunate coincidence, the HKP-2 spectrometer observed ϵ Eri 3 times between 8:43 and 8:48 UT on 1992 November 14, a mere 45 minutes after we obtained a series of optical spectra. A preliminary reduction of the HKP-2 data yielded an S value of 0.494 ± 0.01 (Donahue & Baliunas 1994), which agrees well with our derived value of 0.499.

3. EMPIRICAL TRANSITION DATA

Zeeman analysis requires a variety of atomic data, including transition identifications, Landé-g factors, oscillator strengths, and collisional damping constants. Most of the Fe I transitions in the near-infrared have been identified by Johansson & Learner (1990). Additional line identifications for Fe I and other atoms and ions can be found in Solanki, Biémont, & Mürset (1990). We note that the 1.56825 μm transition is probably mislabeled in both of these references as $e\,^5G_2$–(1/2)[5/2]$^0_3$. To match the observed wavelength, the final state must instead be $e\,^5G_2$–(1/2)[7/2]$^0_3$.

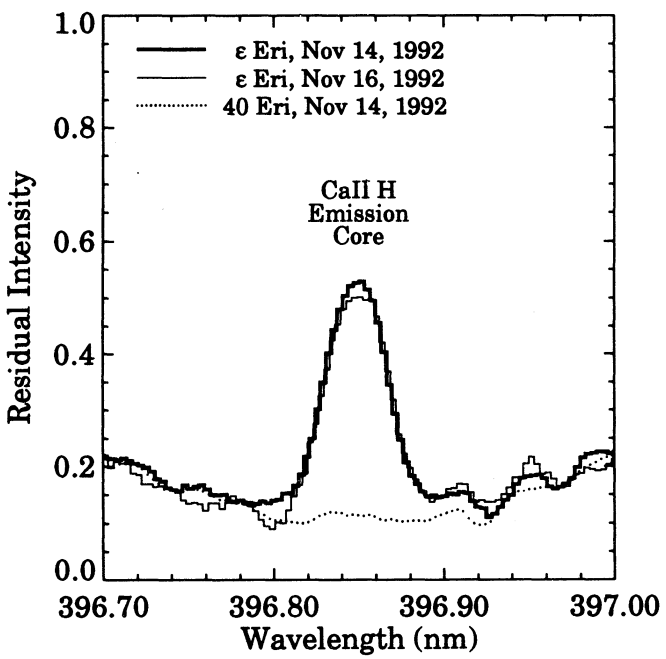

FIG. 3.—Detailed view of the Ca II H cores in Fig. 2, together with an additional profile of ϵ Eri obtained on 1992 November 16. The strong central reversal in the ϵ Eri profiles demonstrates that the star was very active during our Zeeman observations. The inactive star 40 Eri is shown for reference.

We used laboratory values of Landé-g from Sugar & Corliss (1985), when available, and theoretical values otherwise. Most Fe I transitions in the near infrared involve atomic states that are poorly described by the LS-coupling scheme, and for these states, JK-coupling must be used instead (Johansson & Learner 1990). For JK-coupled levels, we used Kurucz's theoretical Landé-g values listed in Johansson & Learner (1990), and for LS-coupled levels, we calculated theoretical Landé-g factors ourselves. Theoretical Landé-g values, especially those calculated assuming pure LS-coupling should be treated with caution until they are verified, since values determined in the laboratory are sometimes quite different (Solanki et al. 1990). More sophisticated theoretical treatments that take into account mixing of quantum mechanical states give better agreement with empirically determined values (Mathys 1990). Apparent errors in $g_{\rm eff}$ were noted by Muglach & Solanki (1992) in their Stokes V analysis of a solar network region. Such discrepancies may arise either when a transition is misidentified or when the assumed value of $g_{\rm eff}$ is in error. Zeeman patterns are independent of the coupling scheme used to describe the state, depending only on J and Landé-g values of the initial and final states.

There are no laboratory measurements of $\log gf$ for the 21 Fe I lines in our study and reliable theoretical values are also unavailable. We empirically determined $\log gf$ values for each line by simultaneously modelling all 21 lines in a spectrum of the quiet Sun at disk center (Livingston & Wallace 1991). The instrumental profile for this FTS spectrum is a sinc function with a full width at half-maximum of 0.0037 nm (0.015 $\rm cm^{-1}$), yielding a resolution of 400,000. This resolution is high enough that we chose to ignore the effects of instrumental broadening in our solar model. Errors introduced by this assumption are negligible when compared with systematic errors in the model profiles themselves. The signal-to-noise ratio of the spectrum is about 1500.

Prior to fitting models and minimizing χ^2, we extracted each line and identified blends that were evident in the line wings. Contaminated pixels were conservatively located by visual inspection, and then ignored in all subsequent analysis. Given the low line density in the infrared, we expected at most one or two significant blends to be hidden in line cores. Poor model fits to lines at 1.55915 and 1.55678 μm may be due to blends that escaped detection. In any case, these two lines were dropped from the analysis. Any remaining weak blends in lines other than the 1.56485 μm line have a negligible effect on our derived parameters, due to the relatively large number of lines being modeled and the small probability of hidden blends. The 1.56485 μm line itself is far and away the most Zeeman sensitive line in our sample, so undetected blends in this line will cause stellar magnetic parameters to be overestimated. Figure 4.1 of Solanki (1993) shows this line in the quiet Sun and the solar network. As in our spectra, a strong blend is apparent in the blue wing and a much weaker blend contaminates the red wing. In sunspots and pores, these blends get stronger, so presumably they grow in stars cooler than the Sun as well. These two blends are excluded from our analysis, but we cannot rule out the possibility of additional weak blends in this line in our spectra.

We modeled the solar spectrum using our LTE spectrum synthesis code and the Holweger-Müller (1974, hereafter HM) atmosphere, $T_{\rm HM}(\tau)$, which has been used extensively to model both the Sun (e.g., Sauval et al. 1984) and (when scaled appropriately) other stars. Rutten & Kostik (1982) have argued that the structure of the HM model serves to mimic non-LTE effects in the context of an LTE analysis. We tested our spectrum synthesis code on optical solar lines with well-determined laboratory values of $\log gf$. Our model profiles tend to be systematically too shallow by about 1% in the cores of the strongest lines, both in the optical and in the infrared. The free parameters of the model cannot be adjusted to correct the discrepancy. We are not certain what causes this problem, but possibilities include NLTE effects, errors in the assumed temperature structure, or an anisotropic turbulent velocity distribution. More study is needed in order to understand how this line core discrepancy affects our derived parameters.

Since we are trying to determine empirical oscillator strengths, we must assume both the relative iron abundance, $\log$ Fe/H, and the microturbulent velocity, ξ. Blackwell, Booth, & Petford (1984) find a value of -4.337 ± 0.017 for $\log$ Fe/H in the Sun, while Holweger et al. (1990, 1991) find values of -4.52 ± 0.09 and -4.50 ± 0.07, respectively. We have selected an intermediate value of -4.40 for our solar models. Our derived $\log gf$ values (described below) are tied to this assumed $\log$ Fe/H of the Sun, but the results can easily be adjusted for small changes in assumed $\log$ Fe/H. Our *stellar* model parameters (discussed in the next section) will not be affected by small errors in our assumed value of $\log$ Fe/H in the Sun, because these errors will be exactly cancelled by corresponding errors in our derived $\log gf$ values.

For consistency with Muglach & Solanki (1992), who also determined empirical $\log gf$ values for Fe I lines in the infrared, we have assumed a depth-independent microturbulence of 0.8 km $\rm s^{-1}$ in the Sun. This assumed microturbulence lies slightly below values deduced from optical studies, which are based on laboratory values of $\log gf$. These studies report values of ξ which range from 0.85 km $\rm s^{-1}$ (Blackwell et al. 1984) to 1.0 km $\rm s^{-1}$ (Holweger, Heise, & Kock 1990). Errors in our assumed value of ξ can lead to small compensatory errors in our derived $\log gf$ values, but our stellar parameters will be isolated from these effects.

With the aforementioned quantities fixed, we proceeded to solve for the remaining parameters by minimizing χ^2, using a nonlinear least-squares minimization routine patterned after the gradient-expansion algorithm described by Bevington (1969). Model profiles were shifted to match the locations of observed profiles and were then multiplied by a linear trend to force agreement between the model and observed continua. All 21 lines were fitted simultaneously, while solving for optimal values of $v_{\rm mac}$, δ_6 (see below), and 21 values of $\log gf$.

Our deduced oscillator strengths are tabulated in Table 3. Column (1) gives the air wavelengths of the transitions based on laboratory measurements (Johansson & Learner 1990; Solanki et al. 1990) and column (2) the lower state excitation potentials. We did not attempt to measure discrepancies between solar and laboratory wavelengths. Column (3) gives the effective Landé-g value of each transition. Our deduced values of $\log gf$ appear in column (4), and the corresponding values from the literature, when available, appear in column (5). Our gf values are 17% $\pm$ 5% larger than those determined by Muglach & Solanki (1992), who used a similar procedure, but analyzed a solar network region, rather than the quiet Sun.

Our assumed and derived stellar parameters for the Sun are summarized in the first entry of Table 4. The parameters in boldface type were derived, while those in normal type were assumed. We did not rotationally broaden our synthetic solar spectrum, since the observed spectrum was taken at disk

TABLE 3

SOLAR OSCILLATOR STRENGTHS

λ (μm) (1)	χ_{lo} (eV) (2)	g_{eff} (3)	log gf [a] (4)	log gf [b] (5)
1.55318	5.708	0.76	−0.45	...
1.55343	5.708	1.99	−0.28	−0.34
1.55377	6.396	0.89	−0.21	...
1.55421	5.708	1.52	−0.50	...
1.55505	6.396	1.60	−0.23	...
1.55514	6.420	0.82	−0.16	...
1.55608[c].....	6.422	0.15	−0.36	...
1.55667	6.424	1.27	−0.36	−0.43
1.55883	5.554	1.37	−0.48	...
1.55937[c].....	5.091	1.61	−1.86	...
1.55989[c].....	6.314	1.63	−0.73	...
1.56042	6.314	1.46	+0.45	...
1.56136[c].....	6.424	1.10	−0.08	...
1.56217	5.603	1.49	+0.50	+0.40
1.56320	5.413	1.65	+0.10	...
1.56485	5.489	3.00	−0.63	−0.68
1.56529	6.318	1.53	−0.03	−0.10[d]
1.56710	6.402	0.54	−0.43	...
1.56732	6.318	0.79	−0.59	...
1.56825	6.443	1.15	−0.25	...
1.56865[c].....	6.318	1.47	+0.21	...

[a] Values of log gf from this work.

[b] Values of log gf from Muglach & Solanki 1992, except for 1.56529 μm transition.

[c] These lines are not used in the Zeeman analysis.

[d] Value of log gf from Solanki et al. 1992b.

center. We also assumed that the Sun was free of magnetic fields, which is essentially true for the region observed. Our v_{mac} of 1.28 km s^{-1} refers to the standard deviation of the (Gaussian) distribution of macroscopic turbulent velocities.

Unsöld (1955) gives a formula for estimating the van der Waal's interaction constant, C_6, but most empirical models of solar and stellar spectra require that C_6 be increased significantly above this theoretical value. Accordingly, we included an enhancement factor, δ_6, for γ_6 as an adjustable parameter in our models of the solar spectrum. In order to best match the solar spectrum we need to boost C_6 by a factor of 10 above the value predicted by Unsöld. This corresponds to a factor of 2.5 increase in the collisional damping constant, γ_6, since $\gamma_6 \propto C_6^{2/5}$. This is at the high end of the range 1.5–2.5 advocated by Holweger et al. (1991). We adopt an enhancement factor of 2.5 for γ_6 in all our subsequent stellar analyses.

4. STELLAR MAGNETIC FIELDS

4.1. *Magnetic Flux Tubes*

In our models, we assume that isolated magnetic regions are uniformly distributed over the stellar surface. Taken together, these regions cover a fraction, f of the stellar surface. The remainder of the stellar surface (the "quiet" component) is assumed to be free of magnetic fields. By analogy with the Sun, we envision magnetic field lines to be organized into thin radial structures (flux tubes), which cluster to form stellar plage and network. Although these structures are concentrated into a broad equatorial band on the Sun, we assume a simpler geometry in which flux tubes are distributed randomly over the entire stellar surface. A radial orientation is expected for flux tubes because they have a lower density than the surrounding photosphere, and thus experience a radial buoyancy force. In a rapidly rotating star, however, the flux tubes may be driven towards the pole by the Coriolis force (Schüssler & Solanki 1992).

To maintain horizontal pressure equilibrium, the gas pressure inside a flux tube must be lower than the external gas pressure to offset the internal pressure contribution by the magnetic field. This means that optical depth unity occurs in deeper layers of the photosphere. The temperature at continuum optical depth unity in the flux tubes may be higher or lower than the temperature in the surrounding photosphere, depending on the diameter of the flux tubes. Radiation maintains small flux tubes in rough thermal equilibrium with the surrounding photosphere, so flux tubes appear hotter. As the size of the flux tube increases, the tubes become optical thick across their diameter and begin to cool, spots being an extreme example. Grossman-Doerth et al. (1994) have argued that flux tubes have an intermediate size (200–400 km), yielding continuum fluxes comparable to the surrounding photosphere as reported by Solanki & Brigljveć (1992). Nonmagnetic portions of active regions may be cooled by radiative losses through the lower opacity flux tubes (Deinzer et al. 1984; Basri, Marcy, & Valenti 1990).

For the sake of simplicity and because there is scant empirical data regarding stellar magnetic flux tubes, we use a fairly simple model in our analysis. We assume that the temperature structure, $T(\tau)$, is the same, both inside the magnetic flux tubes and in the quiet photosphere. This is certainly not the case on the Sun, and our assumption to the contrary is one of the principal sources of uncertainty in our results. Basri et al. (1990) explored the consequences of using a single-component atmosphere in a two-line Zeeman analysis based on the $g_{eff} = 2.5$ line at 846.84 nm. They found that use of a single atmospheric component, rather than two or even three, gives rise to errors of 25% in $|\boldsymbol{B}|f$. The error in $|\boldsymbol{B}|$ should be smaller for the 1.56485 μm line, since the σ components are basically resolved, and therefore less sensitive to model assumptions. Uncertainties in the filling factor are model dependent, however. In fact, Saar & Solanki (1992) considered a hypothetical $g_{eff} = 2.5$ line at 1.6 μm and found that assuming the same temperature structure throughout the atmosphere leads to errors of 10%, 30%, and 15% in $|\boldsymbol{B}|$, f, and $|\boldsymbol{B}|f$, respec-

TABLE 4

STELLAR MODEL PARAMETERS

Star	T_{eff} (K)	log g (cgs)	log Fe/H	δ_6	ξ (km s^{-1})	v_{mac} (km s^{-1})	$v \sin i$ (km s^{-1})	$\lvert\boldsymbol{B}\rvert$ (kG)	f
Sun	5770	4.4	−4.400	**2.5**	0.8	**1.28**	...	...	...
ϵ Eri	**5133**	4.7	**−4.416**	2.5	0.8	**1.32**	1.0	**1.44**	**8.8%**
40 Eri.....	**5072**	4.4	**−4.638**	2.5	0.8	**1.15**	1.0	**1.71**	**2.7**
σ Dra.....	**4943**	4.4	**−4.615**	2.5	0.8	**1.06**	1.0	**1.36**	**1.9**

NOTE.—Derived parameters are in boldface type. Assumed parameters are in normal type.

tively. In § 6.4, we quantify and discuss potential systematic errors specific to our analysis.

4.2. *Spatial Variations in Magnetic Fields*

For most of the work presented here, we assume the magnetic field strength is uniform throughout the magnetic regions. Specifically, $|\boldsymbol{B}|$ is assumed to be independent of spatial location on the stellar surface and also depth in the photosphere. On the Sun, magnetic flux elements have a characteristic, though not unique, field strength (Rabin 1992; Rüedi et al. 1992). Spruit & Zweibel (1978) find that flux tubes are subject to convective instabilities, when the magnetic field strength is below $[8\pi p_e/(1 + \beta_c)]^{1/2}$, where p_e is the total pressure in the external medium (quiet photosphere), β is the gas pressure divided by the magnetic pressure inside the flux tube, and $\beta_c = 1.83$ is the critical value of β for stability in the solar convection zone. Although the exact value of β_c depends on the assumed relationship between the internal and external temperatures (Spruit & Zweibel assumed equality), the notion of a well-defined stability limit is the important point here. Structures with lower field strengths will either contract (for downflows) until the field strength crosses the stability threshold or disperse (for upflows).

As magnetic field lines rise through the photosphere, outwardly directed magnetic flux must remain constant. Hence, the product $|\boldsymbol{B}|f$ is independent of photospheric height. Moreover, β_c varies slowly with height compared to gas pressure, so $|\boldsymbol{B}|$ decreases with increasing height and f increases. We have not included this flaring effect in our analysis, so our derived $|\boldsymbol{B}|$ corresponds to the field strength at the characteristic depth of formation of our magnetically sensitive lines. Grossman-Doerth & Solanki (1990) consider the influence of vertical magnetic field gradients, and find that differences in depth of formation can lead to 50% variations in field strengths derived from different diagnostics.

5. STELLAR ZEEMAN ANALYSIS

In order to distinguish Zeeman broadening from other mechanisms, one must examine one or more Zeeman-sensitive lines for excess broadening relative to the insensitive line(s). This analysis has typically been done with only two or at most a few lines in the past, but using more lines is *very* useful for characterizing sources of nonmagnetic line broadening. The lines used in a Zeeman analysis should span as wide as possible a range of Zeeman sensitivities. It is the contrast in behavior of lines with different sensitivities that unambiguously identifies Zeeman broadening. Figure 4 shows the distribution of effective Landé-g values for the lines used in this analysis. In addition to the Zeeman-sensitive line with $g_{\rm eff} = 3$ and 1.99, there are also a few very insensitive lines with the least sensitive having $g_{\rm eff} = 0.54$. See Table 3 for the $g_{\rm eff}$ values of all the lines used in our analysis. The bulk of the lines lie in the range $1.1 < g_{\rm eff} < 1.8$, giving them moderate Zeeman sensitivities.

We identified and marked blended points in our stellar spectral by visual inspection, much as we did with the solar spectrum. The noise in our stellar spectra made it more difficult to identify blends, but we were able to partially compensate for this disability by intercomparing stellar, solar, and telluric spectra. We plotted all three of our stellar spectra together with spectra of the quiet Sun (Livingston & Wallace 1991) and Earth's atmosphere (Livingston & Wallace 1991). A printed sunspot spectrum (Wallace & Livingston 1992) was used to identify features characteristic of cooler atmospheres.

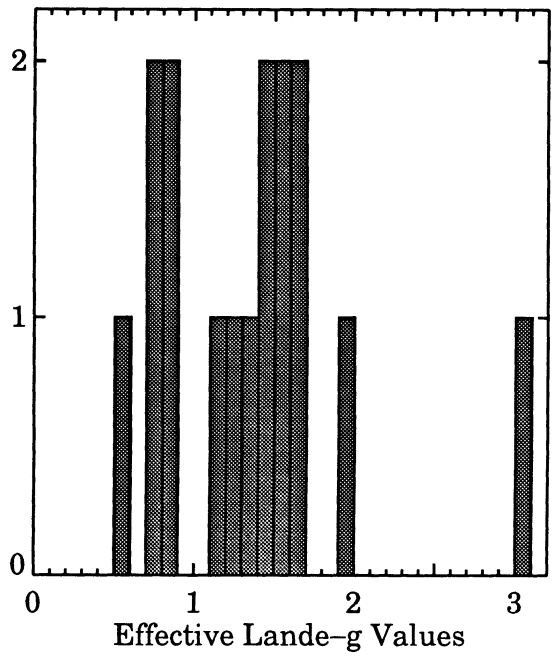

FIG. 4.—Distribution of effective Landé-g values for the lines used in the Zeeman analysis. The sample includes a few lines with low magnetic sensitivity, one with very high sensitivity, and the rest with sensitivities comparable to the best optical diagnostics.

Weak features appearing in all three stellar spectra and either the sunspot or the quiet Sun were judged to be real blends, rather than noise. Since blended pixels were identified simultaneously in all three of our stellar spectra, a similar set of pixels was retained for subsequent analysis. A few additional pixels were excluded in individual spectra, if these pixels seemed highly discrepant, when compared with the same pixels in all other spectra. Identified blends were ignored throughout the χ^2 analysis. A few blends were undoubtedly retained in the Zeeman analysis, but these blends are weak compared to the strength of the lines they contaminate. Nonetheless, the presence of untreated blends certainly gives rise to small, but systematic, errors in our derived model parameters. If any blends are buried in the line cores, they must be fairly weak, since observed line cores are at most 2% deeper than model line cores.

Unblended points within 0.5 nm of line center were used to map the model continuum onto the observed continuum. The continuum threshold was set at 2% of the residual line depth. For example, a model profile with a residual intensity in the line core of 0.75 would have a continuum threshold of 0.995. The continuum region for this line would consist of all wavelengths for which the residual intensity of the *model* profile lay between 0.995 and 1.000. For each observed profile, a straight line was fitted to all unblended points in the continuum region. The corresponding model profile was then multiplied by the linear function to match the observed and model continua.

5.1. *Assumed Parameters*

We modeled our FTS spectra of ϵ Eri, 40 Eri, and σ Dra, using the same radiative transfer code that we used to model the Sun, but with a different set of free parameters. In particular, we allowed the magnetic field parameters ($|\boldsymbol{B}|$ and f) to float. We fixed the atomic parameters, δ_6 and $\log gf$, to values

determined in our analysis of solar spectrum. In our stellar models, the free parameters are effective temperature ($T_{\rm eff}$), relative iron abundance (log Fe/H), macroturbulence ($v_{\rm mac}$), magnetic field strength ($|\boldsymbol{B}|$), and surface covering fraction (f). These five free parameters are constrained by 16 observed line profiles. As in our solar model, we fix the microturbulence (ξ) at 0.8 km s^{-1}. Surface gravity (log g) is either fixed at a value taken from the literature (ϵ Eri) or tied to $T_{\rm eff}$, as discussed below.

We use scaled versions of the HM solar atmosphere to describe the temperature structure, $T(\tau)$, of our target stars. The atmosphere of each star is characterized by an effective temperature, $T_{\rm eff}$, such that the temperature at each optical depth is given by

$$T(\tau) = \frac{T_{\rm eff}}{5770\ \rm K} \times T_{\rm HM}(\tau)\ , \qquad (3)$$

where $T_{\rm HM}(\tau)$ is the solar atmosphere tabulated by HM, and 5770 K is the assumed effective temperature of the Sun. The same atmosphere is used in both the magnetic and quiet components. (This restriction is relaxed in §§ 6.4 and 7.3, which consider two-component models.) Self-consistent optical depths are obtained for the desired temperature structure by solving implicit relations for gas pressure, electron pressure, and ionization at each depth. In practice, the pressure structure is obtained via bilinear interpolation in a grid of precomputed solutions.

Drake & Smith (1993, hereafter DS) infer a surface gravity of 4.75 $\pm$ 0.1 for ϵ Eri, based on the collisionally broadened wings of the Ca I 6162 Å line. This value lies just outside our interpolation grid of stellar atmospheres. As a result, we used log g = 4.7, which is close enough to the value of DS that the difference is of no consequence. For 40 Eri and σ Dra, we tie surface gravity to effective temperature using an empirical fit to eclipsing binary data (Harmanec 1988). Significant deviations from Harmanec's relation are possible, though. For example, log g is underestimated by 0.12 (30%) for the Sun. Nonetheless, Harmanec's empirical fit provides a good statistical estimate of unmeasured surface gravities. Harmanec's relation yields near solar gravities for our early K stars. Poorly determined gravities are a significant source of error in our analysis, as will be discussed in § 6.4.

As in our solar model, we assume a microturbulence of 0.8 km s^{-1}. Drake & Smith (1993) deduce a microturbulence of 1.25 $\pm$ 0.1 km s^{-1} for ϵ Eri, which is somewhat higher than our assumed value. Their microturbulence is dependent, however, on the behavior of a single Ca I line at 5867.57 Å (see Fig. 3 of DS). If this line is ignored, the remaining six Ca I lines studied by DS are equally well described by any microturbulent velocity in the range 0.8–1.2 km s^{-1}. In the context of their analysis, a lower microturbulence implies a higher calcium abundance, and therefore a lower surface gravity, which is more in keeping with Harmanec's (1988) relation.

Finally, we fix the projected equatorial velocity (v sin i) at a small, but otherwise arbitrary value of 1.0 km s^{-1}, which happens to match the v sin i adopted by Marcy & Basri (1989) for ϵ Eri and σ Dra. All three of our target stars have v sin $i < 2.0$ km s^{-1}, making it difficult to even detect stellar rotation, but making them good candidates for Zeeman analysis. If we allow v sin i to float as a free parameter, it is consistently driven to zero for all three stars. This may indicate that in the absence of a strong rotational constraint, the model is using v sin i to correct for a systematic problem in line shape. Specifically, by driving v sin i to zero, the model line cores are sharpened. As discussed in § 6.4, assuming v sin i = 1.0 km s^{-1} has a negligible effect on all derived parameters, except macroturbulence.

5.2. *Modeling Technique*

The transfer of Stokes components through a stellar atmosphere is governed by a set of four coupled partial differential equations (Unno 1956; Landi Degl'Innocenti & Landi Degl'Innocenti 1972; Jefferies, Lites, & Skumanich 1989; Rees, Murphy, & Durrant 1989). We use a fourth-order Runge-Kutta integration scheme to solve these equations for the emergent intensity profile. More efficient numerical schemes exist (Rees et al. 1989), but the Runge-Kutta scheme is sufficiently fast for our purposes. We compute intensity profiles at seven μ angles, chosen to divide the projected stellar disk into equal area annuli.

We ignore magneto-optical effects, which primarily affect the Stokes Q and U components, but may still be significant in our case, due to the large splitting of the σ components (Landolfi & Landi Degl'Innocenti 1982). Further study is needed to assess the importance of magneto-optical effects on magnetic parameters deduced with the 1.56485 μm line.

Rotation and isotropic Gaussian macroturbulence are treated together by means of "disk integration" in which intensity profiles are numerically integrated over the stellar disk (Gray 1992). A nonisotropic macroturbulence (e.g., radial tangential) would probably yield better model fits, but at the expense of an additional free parameter. We use a new disk integration technique, that will be described in detail in a separate paper (Valenti & Anderson 1995). Briefly, the integration within each annulus is reformulated as two convolutions. This greatly reduces the amount of time required to achieve the desired level of accuracy. Moreover, the convolution kernels account analytically for the thickness of each annulus, making it completely unnecessary to interpolate intensity profiles during the integration. In this manner, we are able to achieve more than adequate precision (maximum error of 0.2%) with intensity profiles calculated at only seven μ values.

To account for line broadening by the spectrograph, we convolved model flux profiles with a sinc function with a full width at half-maximum of 0.015 nm. We took this width for the instrumental profile directly from the spectrograph control program, after entering the temperature and humidity in the spectrograph room. We made no effort to directly measure the width or shape of the instrumental profile, but the actual shape of the instrumental profile is thought to be reasonably close to the predicted shape (Hall et al. 1979).

6. RESULTS

6.1. *Model Profiles*

We modeled each of our spectra, following the procedure described above. The free parameters in the stellar models were effective temperature, iron abundance, macroturbulent velocity, magnetic field strength, and surface covering fraction of magnetic fields. Values determined for these stellar parameters are listed in boldface type in Table 4. The remaining parameters in the table were fixed at assumed values during the modeling procedure. Parameters of our solar model are shown in the first row, for comparison.

Figure 5 shows observed and model profiles for five lines in our spectrum of ϵ Eri. Lines increase in strength from top to bottom, with the normalized continuum of each line progres-

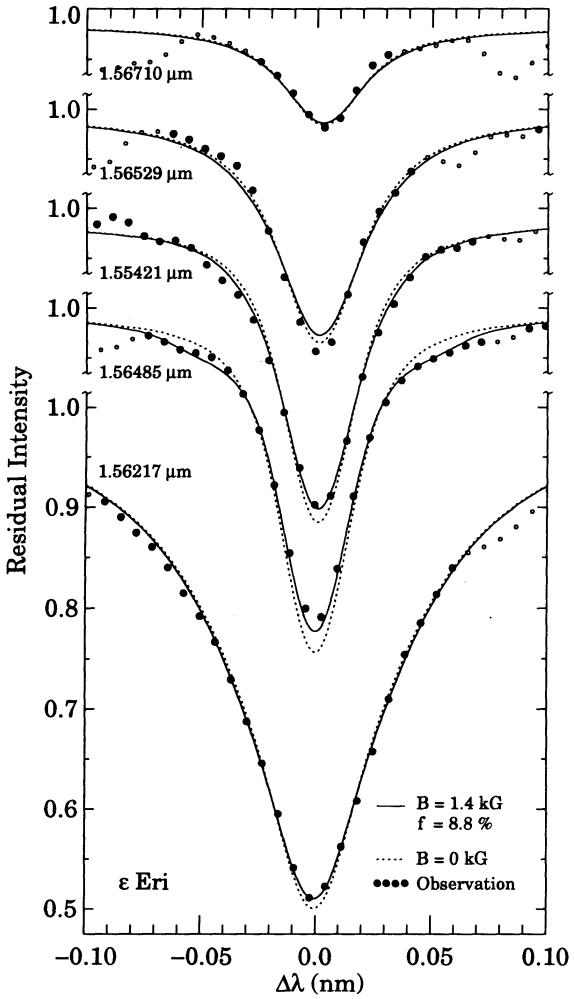

FIG. 5.—Comparison of observed residual intensities and model profiles predicted using our adopted parameters for ϵ Eri. Only five of the 16 lines used in the Zeeman analysis are shown, ordered by line strength. All profiles have the same vertical scale, but successive profiles displaced vertically by 0.1 continuum units. Filled circles were used in the model fitting procedure, while unfilled circles (blends) were ignored. The solid profiles illustrate the predictions of our adopted model for ϵ Eri (see Table 4), while the dashed profiles shows what the spectrum would look like if the star had no magnetic field.

sively offset by 0.1 continuum units. These profiles are characteristic of the full set of 16 Fe I lines used in the model-fitting procedure. The five lines span the full range of line strength, and their RMS residuals are neither the best, nor the worst, of the lot. The line at 1.56485 μm is the most magnetically sensitive ($g_{\rm eff} = 3.0$) line in our sample, while the line at 1.56710 is the least sensitive ($g_{\rm eff} = 0.54$). Circles indicate the observed profiles, with unfilled circles designating those points contaminated by blends, and therefore ignored, a priori, during the modeling procedure. Solid profiles show the fit attained by our adopted model of ϵ Eri (see Table 4). Dashed profiles were generated by setting $|\boldsymbol{B}|$ and f to zero, and using our adopted nonmagnetic parameters (without reoptimizing).

The model fit to ϵ Eri is quite good with an RMS residual of 0.76%, corresponding to a reduced χ^2 of 2.72 for 1016 observed spectrum points. The RMS residual is slightly larger than the 0.47% random noise in the sepectrum, in keeping with the small systematic errors discernable in the model fits. Larger errors in the lines are cancelled to some extent by good fits in the adjacent continuum, however, making it dangerous to blindly interpret these statistics. The fit to 40 Eri has an RMS residual of 0.80% and a reduced χ^2 of 1.71. Despite the increased noise in the spectrum (0.63%) compared to ϵ Eri, the RMS is basically the same, so systematic errors are still significant. For σ Dra, however, the RMS residual is 1.00% with a reduced χ^2 of 0.84, indicating that the increased random noise in the spectrum (1.12%) exceeds systematic errors in the model. In calculating χ^2, we subtracted 53 from the total number of pixels to get the degrees of freedom. (In addition to the five astrophysical free parameters, each model has three alignment parameters per line: one to align the model wavelength scale and two to match the model to the observed continuum.)

Figure 6 shows residuals calculated by subtracting the $|\boldsymbol{B}| = 0$ profiles in Figure 5 (*dashed curves*) from both the observed profiles (*circles*) and the profiles predicted by our adopted model of ϵ Eri (*solid curves*). The residuals show perturbations that in our models are attributed to magnetic fields. The vertical scale is the same for each residual plot, with a tick

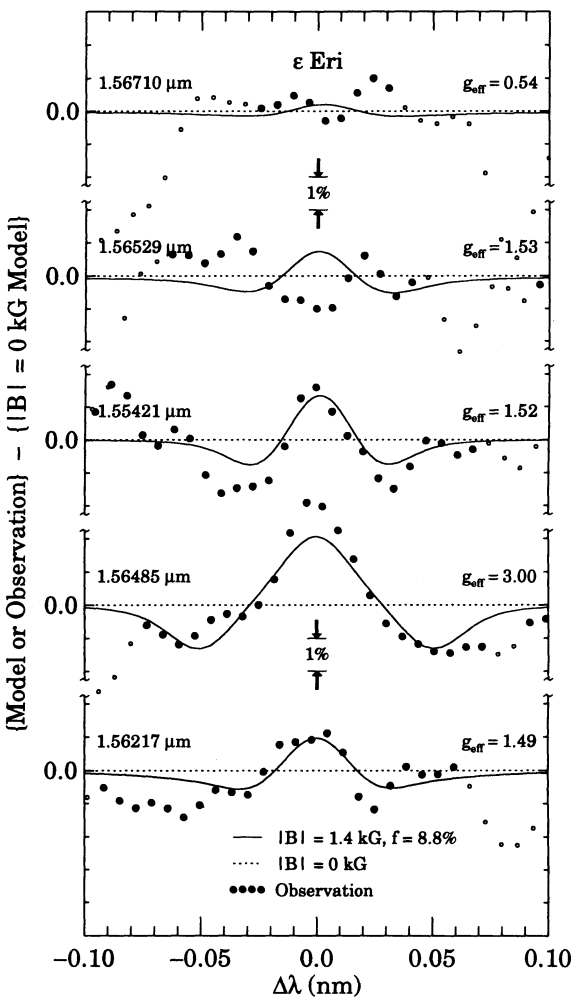

FIG. 6.—Residual profiles showing both the predicted effects of a magnetic field and actual perturbations observed in ϵ Eri. The residuals were constructed by subtracting the $|\boldsymbol{B}| = 0$ model profiles from both the observed and magnetic model profiles in Fig. 5. All residual profiles have the same vertical scale, but successive lines are displaced vertically by 0.05 continuum units. Tick marks on the ordinate indicate steps of 1% relative to the continuum. Effective Landé-g values are indicated for each line, and plot symbols are as in Fig. 5.

mark corresponding to a discrepancy of 1% relative to the continuum. There is a reasonable correspondence between the observed residuals and those predicted by our model (as there should be), but systematic errors clearly remain at the 1% level. Line cores tend to be off in one sense (either too high or too low), while points in the profile at $\Delta\lambda \sim \pm 0.025$ nm are off in the opposite sense. Similar errors exist in our fits to spectra of 40 Eri and σ Dra, although the discrepancies are harder to see in the noisier spectrum of σ Dra. These systematic errors define the limits of our current understanding of atmospheric physics in late-type main-sequence stars, and set limits on the accuracy with which magnetic fields can be measured.

There is a correlation between the excitation potential of the ground state and the sense of the systematic errors in the model fits. Model fits tend to be too deep in the cores of lower excitation lines, while the opposite is true for lines with higher excitation potentials. In the context of our infrared Zeeman analysis, we have seven "low-"excitation lines with 5.51 eV $< \chi <$ 5.71 eV and nine "high-"excitation lines with 6.31 eV $< \chi <$ 6.45 eV (see Table 3). The systematic nature of the core discrepancy can be seen in Figure 6 by comparing the observed line cores (*circles*) with our adopted model profiles (*solid curves*). The top two transitions have high excitation potentials and the model cores are too shallow, whereas the bottom three transitions have lower excitation potentials and the model cores are too deep. We have also encountered these errors when modeling lower excitation (2–4 eV) Fe I lines in the optical, except that the discrepancy in the core changes its sense at 3 eV rather than 6 eV.

The systematic errors in lower excitation lines are reminiscent of the perturbations due to magnetic fields, which is a serious concern. If model parameters are adjusted to match high-excitation lines, then systematic errors in lower excitation lines may very well mimic the effects of a magnetic field. The danger is evident for two-line Zeeman analyses in which the excitation potential of the magnetically sensitive line is substantially lower than the excitation potential of the insensitive line (as is the case for the [0.77483, 0.84684 μm] and [1.56485, 1.56529 μm] line pairs, both of which have been used in the literature). Despite these concerns, we believe the current multiline analysis overcomes these problems. The Zeeman effect in the core of our most sensitive line (1.56485 μm) is twice the magnitude of the systematic error. Moreover, the splitting of the σ components places them safely outside the portion of the profile affected by the systematic errors. In our sample of lines, there is a weak correlation between excitation potential and $g_{\rm eff}$. The mean $g_{\rm eff}$ for low-excitation lines exceeds the mean $g_{\rm eff}$ for high-excitation lines by 0.56, which will bias the analysis toward positive magnetic field detections. However, both excitation bins have lines that span a large, overlapping range in $g_{\rm eff}$, which helps mitigate systematic errors. Finally, we do not detect strong magnetic fields on the two inactive stars in our sample. In fact, the weak magnetic fluxes for these stars (25% of the flux detected on ϵ Eri) probably demonstrate the combined effects of random noise and systematic modeling errors.

6.2. *Stellar Properties*

Of primary interest are the magnetic parameters in the final two columns of Table 4. We definitely detect a magnetic field on ϵ Eri, but the total magnetic flux ($|\boldsymbol{B}|f = 0.127$ kG) is much lower than what has been found in previous optical studies. We will argue in § 7.2 that our infrared result is accurate, and that optical measurements have overestimated the true flux. For the two inactive stars, 40 Eri and σ Dra, we find even lower surface covering fractions and magnetic fluxes. A covering fraction of 2.7% for 40 Eri is at the detection threshold, which is noteworthy because the star was particularly active during our observations (see § 7.2). For σ Dra, our deduced covering fraction of 1.9% is really a nondetection, given the poorer quality of the spectrum. As discussed in § 6.1, the small positive results for the two inactive stars may well be due to systematic errors in the analysis.

Figure 7 shows the magnetically sensitive ($g_{\rm eff} = 3.0$) line at 1.56485 μm for each target star. Observed points are shown as circles (filled for unblended points, unfilled for blends), while the best-fitting models are given by the solid profiles. Inferred magnetic field strength and surface covering fraction appear to the right of each profile. Dotted profiles were obtained by

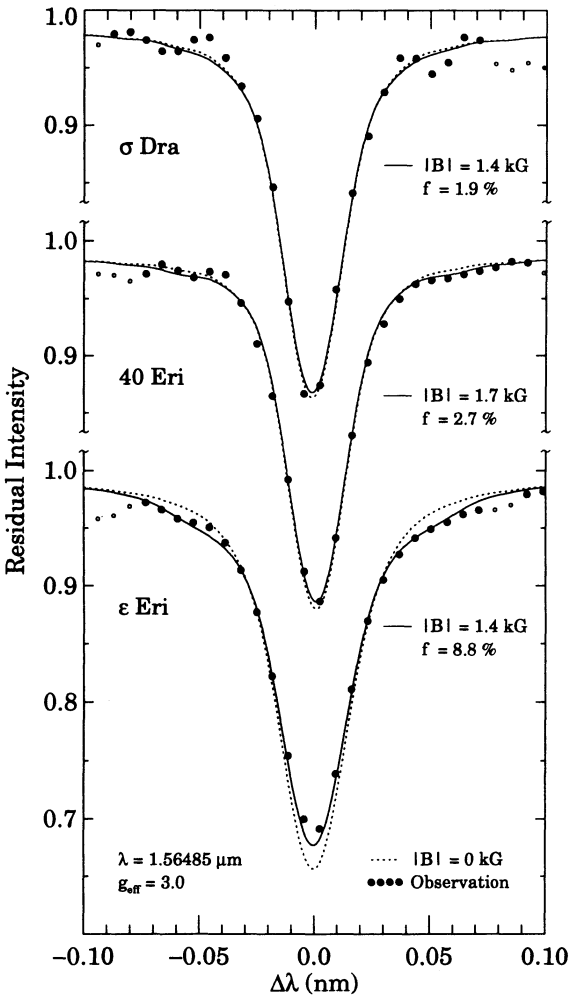

FIG. 7.—Profiles for the most magnetically sensitive of the 16 lines simultaneously fitted in our Zeeman analysis. The inferred Zeeman signal in the line core and in the wings is stronger in ϵ Eri than it is in the two inactive stars. The absence of large perturbations in the inactive stars indicates that the observed perturbations in ϵ Eri are not due to unidentified blends or modeling errors. The magnetic parameters of the best-fitting model for each star are given to the right of each profile. Solid profiles show the best-fitting magnetic model, while the dashed profiles show what the line would look like if the star had no magnetic field. Solid circles indicate observed data used in the modeling procedure, while open circles are blends that were ignored.

setting $|\boldsymbol{B}| = 0$ in the best-fitting model, thereby making the difference between the solid and dotted profiles a measure of the Zeeman effect in our models. The wings of ϵ Eri are clearly enhanced relative to the $|\boldsymbol{B}| = 0$ model, whereas the wings of 40 Eri and σ Dra show little or no enhancement. *This demonstrates that the enhanced wings seen in ϵ Eri are not an artifact of the modeling procedure, nor are they caused by weak blends, but are instead due to magnetic fields.*

Of the spectral lines included in our analysis, magnetic fields have the largest effect on the $g_{\rm eff} = 3$ line at 1.56485 μm. For our adopted model of ϵ Eri ($|\boldsymbol{B}| = 1.44$ kG, $f = 8.8\%$), the residual intensity of this line changes by a maximum of 1.2% in the wings and 1.8% in the core (Fig. 6, second line from the bottom). Basri & Marcy (1994) have recently explored Zeeman enhancement of equivalent widths as a magnetic diagnostic on rapidly rotating stars. For the 1.56485 μm line, we note that the equivalent width in the line core ($|\Delta\lambda| < 0.03$ nm) decreases by 6.3 mÅ, while the equivalent width in both of the wings combined increases by 8.9 mÅ. Here the "core" is defined as the central portion of the line between the points at which the $|\boldsymbol{B}| = 0$ profile crosses the best-fitting magnetic model. Overall, the equivalent width of the 1.56485 μm line increases by 2.6 mÅ, which corresponds to a net change of +1.6%. At the other extreme, the $g_{\rm eff} = 0.54$ line at 1.56710 μm (topmost spectral line in Fig. 6) changes relatively little in the presence of a magnetic field. The maximum change in the wings is 0.1%, while the core gets shallower by 0.2%. The equivalent width increases by only 0.06 mÅ, corresponding to an overall enhancement of 0.04%. Notice that the changes in the profile features and equivalent widths do not scale directly with $g_{\rm eff}$. The actual sensitivity of a particular line depends on a number of factors, including the spacing of the (many) σ components and the amount of desaturation, as the σ components separate from the π components and each other (Basri et al. 1990). Basri & Marcy (1994) concluded that the magnetic field on ϵ Eri is too weak to be detected by equivalent width changes.

We now turn to the nonmagnetic stellar parameters (listed in Table 4) deduced in our analysis. We find a temperature of 5133 K for ϵ Eri, which agrees well with other recent determinations. On the basis of a multiline analysis in the optical, Drake & Smith (1993) deduced a temperature of 5180 ± 50 K, which agrees our result. In fact, if we use the gravity dependence of our models (see § 6.4) to extrapolate our model to their gravity of 4.75, we find a very similar temperature of 5186 K. Gray & Johanson (1991) determined a temperature of 5122 K, based on $B-V$ color, and a temperature of 5152 K from the ratio of the depths of the 625.183 nm V I and 625.257 nm Fe I lines. The results of many earlier studies are summarized in Table 1 of DS. Most find lower temperatures (around 5000 K), but these works are almost all based on photometric data, which is a rather crude diagnostic of temperature. For σ Dra, Gray & Johanson (1991) found a temperature of 5349 K (from $B-V$ colors) and 5371 K (from V I/Fe I line ratio). The same line ratio and temperature calibration was used by Gray et al. (1992), who found an average temperature of 5381 K for 56 spectra of σ Dra. Our derived temperature of 4943 K is much lower. As is discussed below, this discrepancy in temperature can be attributed to uncertainty in the surface gravity of σ Dra.

After subtracting our assumed solar iron abundance [log (Fe/H) = −4.40] from column (3) of Table 4, we find relative iron abundances of −0.02, −0.24, and −0.22 for ϵ Eri, 40 Eri, and σ Dra, respectively. Both inactive stars are metal poor, as would be expected of very old stars, but surprisingly, ϵ Eri is also slightly metal poor, despite its apparent youth. In fact, previous studies of ϵ Eri yielded even lower values of [Fe/H], namely -0.09 ± 0.05 (DS) and -0.23 ± 0.07 (Steenbock 1983). For σ Dra, our [Fe/H] of −0.22 agrees reasonably well with the value of −0.30 obtained by Marcy & Basri (1989).

Of the nonmagnetic parameters in Table 4, the most intriguing is effective temperature. Temperature apparently *increases* toward later spectral type, rather than decreasing, as one might intuitively expect. Our derived temperatures do depend on certain model assumptions. In particular, ϵ Eri (K2 V) has a higher assumed gravity and is more active than 40 Eri (K1 V). We show in § 6.4 that assuming a higher gravity leads to hotter model atmospheres. Incorrectly assuming that hot magnetic regions are at the same temperature as the quiet photosphere also yields a higher apparent temperature. It is entirely possible, however, that our derived temperatures are correct and it is the spectral types which are misleading. Spectral types are commonly thought of as temperature diagnostics, but the line ratios used in assigning spectral types are also affected by iron abundance, gravity, and chromospheric activity. In light of this, it is not surprising that the general correspondence between spectral type and temperature breaks down for particular stars separated by only one or two spectral subclasses. For example, Gray & Johanson (1991) list temperatures (based on $B-V$ colors) for three K0 V and four K2 V stars. Even with such small samples, the temperatures span 150 K within each spectral type. Our temperature of 4942 K for σ Dra is exceptionally cool for a K0 V star, casting some doubt on this particular result. Although the noise was somewhat higher in σ Dra, compared with the other two stars, it seems unlikely this could lead to such a large an error in temperature. The discrepancy can be explained, however, if the surface gravity on σ Dra is at least 4.7, rather than the value (log $g = 4.4$) assumed in our analysis.

6.3. *Random Errors*

Random noise in observed spectra gives rise to errors in derived model parameters. These errors are best characterized by a joint confidence region, calculated from the covariance (inverse curvature) matrix (Press et al. 1986). The resulting five-dimensional ellipsoid is difficult to present, however. So instead, we calculate confidence intervals separately for each parameter by taking the square root of elements on the main diagonal of the covariance matrix. These formal 1 σ confidence intervals for parameters of our ϵ Eri model are tabulated in the first row of Table 5. The fractional uncertainties in $|\boldsymbol{B}|$ and f are 5% and 11%, respectively. Incorrect formal uncertainties appeared in an earlier conference proceeding (Valenti, Marcy, & Basri 1994), due to an invalid assumption in the gradient expansion algorithm (Bevington 1969) that was used. The calculation of uncertainties in Bevington's "CURFIT" subroutine assumes that $\lambda \ll 1$ at convergence, which is not always true. In this context, λ is the weighting factor between a pure gradient search ($\lambda \gg 1$) and minimization of a Taylor series expansion ($\lambda \ll 1$).

We compared formal errors from the covariance matrix with standard deviations of parameters determined in a Monte Carlo experiment. Thirty synthetic "observations" were generated by adding normally distributed noise with a standard deviation of 0.5% to a noiseless model spectrum of ϵ Eri. The synthetic spectra were convolved with a sinc function and

TABLE 5

ERRORS IN ϵ ERIDANI PARAMETERS DUE TO NOISE AND MODEL ASSUMPTIONS

Model	$T_{\rm eff}$ (K)	log Fe/H	$v_{\rm mac}$ (km s^{-1})	$\lvert B\rvert$ (kG)	f	χ^2
Formal Errors[a]	9.0	0.0026	0.039	0.058	0.84%	...
Monte Carlo[b]	7.6	0.0023	0.028	0.044	0.66	...
Adopted Model	5132.6	−4.4157	1.319	1.445	8.83	2.73
$v \sin i = 0$ km s^{-1}	5133.8	−4.4151	1.412	1.498	8.43	2.73
$v \sin i = 2$ km s^{-1}	5134.7	−4.4152	0.983	1.489	8.90	2.74
$\log g = 4.55$ (cgs)	4960.3	−4.4456	1.407	1.553	9.60	2.78
$\log g = 4.40$ (cgs)	4808.8	−4.4605	1.498	1.639	10.36	2.70
$T_{\rm act} = 6000$ K	5079.8	−4.4017	1.332	1.429	6.40	2.72

[a] Confidence intervals (1 σ) calculated from covariance (inverse curvature) matrix.
[b] Confidence intervals (1 σ) calculated from Monte Carlo experiment.

binned in wavelength to match the FTS observations. We then analyzed each synthetic spectrum, using our standard Zeeman analysis procedure, ignoring points that were identified as blends in the true spectrum. Standard deviations of the resulting set of parameters appear in the second row of Table 5. Confidence intervals determined in the Monte Carlo experiment are actually smaller than the formal uncertainties by a factor of about 0.8, indicating a problem in the error analysis at this level. To be conservative, we adopt the larger formal uncertainties from the covariance matrix as our estimate of errors due to random noise in the spectrum of ϵ Eri.

It is commonly argued (Gray 1984; Saar 1988) that random noise in observed profiles gives rise to correlated errors in $|B|$ and f, such that each of these quantities is known less accurately than the combination $|B|f^{0.5}$. We have tested this supposition and find that for our analysis, $|B|f^{0.80}$ is the most accurately determined quantity. This relationship must be specified properly to allow proper reconstruction of the joint confidence region. We calculated a grid of ϵ Eri models with field strengths between 0 and 3 kG and surface covering fractions between 0% and 20%. The χ^2 surface determined by comparing these models with the observed spectrum of ϵ Eri has a "valley" in the $(|B|, f)$ plane that follows the curve defined by $|B|f^{0.8} = 0.21$ kG.

The same result can be obtained directly from the covariance matrix, once we assume (or in this case know) that the valley follows a curve of the form

$$|B|f^{\gamma} = |B|_{\rm obs} f^{\gamma}_{\rm obs} , \quad (4)$$

where the subscripted constants on the right-hand side of the equation refer to quantities determined in the Zeeman analysis. Solving for $|B|$ and taking a derivative with respect to f gives an expression for the slope of the curve following the valley in χ^2 at the point of our solution. But this slope is just the slope of the major axis of the joint confidence ellipse for $|B|$ and f, obtained (see Press et al. 1986) from the covariance matrix. Solving for γ gives 0.80 in excellent agreement with the results of the brute force grid calculation described above. The joint confidence ellipse can also be used to determine 1 σ confidence limits along the $|B|f^{0.8} = 0.207$ kG curve and perpendicular to it. The formal uncertainty perpendicular to the valley (i.e., in the quantity 0.207 kG) is very small, amounting to only 0.1%. Clearly, other systematic effects dominate errors in this quantity. Along the valley, however, random errors do play a significant role. The formal 1 σ confidence interval *along the valley* extends between $(|B|, f) = (1.31$ kG, 10.0%) and (1.60 kG, 7.8%). Note that by considering correlated errors in $|B|$ and f, the range of $|B|$ values contained in the confidence region increased by a factor 2.5, illustrating the importance of properly treating joint uncertainties.

6.4. *Systematic Errors*

It is also important to assess potential systematic errors that may arise due to invalid model assumptions, since these errors can be substantially larger than random errors. To study this issue, we relaxed or changed certain model assumptions and then reanalyzed our observed spectrum of ϵ Eri. Differences in the new derived parameters and our adopted parameters provide an estimate of possible systematic errors. The results of all of these tests are summarized in Table 5.

We began by considering the effects of adopting a particular value of $v \sin i$ in our analysis of ϵ Eri. Macroturbulence and low values of $v \sin i$ have very similar effects on line profiles, so distinguishing between these two broadening mechanisms (in slowly rotating stars) requires excellent models and very high resolution spectra with low noise (Marcy & Basri 1989). We verified this by reanalyzing ϵ Eri with $v \sin i$ set to 0 and then 2 km s^{-1}, rather than our adopted value of 1.0 km s^{-1} (see § 5.1). The resulting parameters appear in Table 5 beneath our adopted model parameters. Most parameters changed by less than their random errors, but as expected, $v_{\rm mac}$ changed substantially to offset the change in $v \sin i$. Fixing $v \sin i$ at 1.0 km s^{-1} introduces the potential for errors as large as 0.3 km s^{-1} in $v_{\rm mac}$, but does not significantly increase the errors in other parameters beyond levels expected due to random noise. The same result presumably holds for 40 Eri and σ Dra.

The surface gravities of our target stars are also poorly known (see § 5.1). We reanalyzed ϵ Eri with two other plausible values of $\log g$, namely 4.40 and 4.55, instead of our adopted value of 4.70. The lower value, which we adopted for our two inactive stars, is based (statistically) on masses in binary systems (Harmanec 1988). The value of 4.55 is midway between $\log g = 4.40$ and our adopted value. As shown in Table 5, all model parameters changed by substantially more than their formal errors. The most significant change was in temperature, which decreased by 110 K for each drop of 0.1 in $\log g$. Steenbock (1983) noted a similar effect, although in our case the magnitude of the effect is larger by a factor of 2. The magnetic parameters, $|B|$ and f, increased by 70 G and 0.5%, respectively, for a drop of 0.1 in $\log g$. Errors in $\log g$ (typically ± 0.3) are clearly a significant source of error in derived magnetic parameters. Moreover, these errors in $|B|$ and f *do not cancel* in the products $|B|f$ and $|B|f^{0.5}$, as would be the case for errors due to poor spectral resolution or excessive noise. The model

with log g = 4.4 (cgs) actually has a slightly lower χ^2 than our adopted model, so that on the basis of our data alone, this is the preferred model. The gravity diagnostic used by DS is presumably more sensitive than the lines studied here, but we adopt a significantly lower microturbulence than DS. More information is needed to choose between the two models, so for now we simply point out the potential errors in derived stellar parameters that may result from a poorly known gravity.

In a final test to quantify possible systematic errors, we considered how derived model parameters are affected by altering the atmosphere in the magnetic component. Specifically, we let the effective temperature characterizing the quiet component float, but fixed the effective temperature of the magnetic component at 6000 K. The resulting parameters appear in Table 5. For the atmsphere of the magnetic component, we used an HM solar model scaled to an effective temperature of 6000 K. A hot HM model is far from an adequate description of stellar flux tubes, but it does mimic the higher temperatures at continuum optical depth unity that occur in some real flux tubes. As one might expect, the derived temperature of the quiet component decreased (by 53 K) to compensate for the reduced equivalent widths in the hotter magnetic component. Magnetic field strength was *not* significantly affected because it depends primarily on the locations of resolved σ components, which in turn depend only on magnetic field strength. Magnetic fields derived from optical diagnostics, however, probably are subject to systematic errors because the σ components are unresolved and therefore easily confused with line shape changes due to the presence of a second atmospheric component. In contrast to $|\boldsymbol{B}|$, the derived surface covering fraction, f, does depend on the choice of atmosphere for the magnetic regions. In the two-component model, the covering fraction decreases by a factor of 0.73 (from 8.8% to 6.4%), which is close to the ratio of continuum fluxes in the two atmospheres (quiet over hot). See Rüedi et al. (1994) for another preliminary attempt at modeling ϵ Eri with two temperature components.

On the basis of these tests, we conclude that invalid model assumptions may lead to systematic errors as large as 300 K in $T_{\rm eff}$, 0.04 in log (Fe/H), 0.3 km s^{-1} in $v_{\rm mac}$, 0.2 kG in $|\boldsymbol{B}|$, and 2.5% in f. The error estimate for f is likely to be representative of actual systematic errors, given that we only used a single atmospheric component in our analysis. On the other hand, errors in the other parameters will be smaller than the above estimates, if we have selected $v \sin i$ and log g wisely. In particular, $|\boldsymbol{B}|$ is almost independent of model assumptions because $|\boldsymbol{B}|$ depends only on the locations of the σ components, which are well defined by the 1.56485 μm line. Optical Zeeman analyses, however, are quite sensitive to model assumptions, since σ components are unresolved in the optical. This undoubtedly accounts for some of the large scatter in field strengths reported in the literature (see § 7.1). Although infrared diagnostics of $|\boldsymbol{B}|$ are relatively insensitive to model assumptions, they still have significant errors due to random noise in the spectrum (see above). Systematic error estimates for our two inactive stars should be comparable to those discussed above for ϵ Eri, since they are modeled under similar assumptions.

7. DISCUSSION

7.1. *Comparison with Previous Results*

It is worth remembering that with one exception, all existing Zeeman studies of cool stars have been based on the analysis of two or at most a few lines. Only Mathys & Solanki (1989) have considered a large number of optical lines, and their regression analysis of various line widths and depths is an extreme simplification of physical line transfer. The modeling errors that are apparent in our multiline analysis are presumably less than the errors that have been present in all previous Zeeman work. By simultaneously analyzing many lines, we are able to quantify possible systematic errors in measured magnetic properties.

TABLE 6

SELECTED MAGNETIC FIELD MEASUREMENTS FOR ϵ ERIDANI

$\lvert\boldsymbol{B}\rvert$ (kG)	(f)	$\lvert\boldsymbol{B}\rvert f$ (kG)	λ (μm)	Reference
1.2	67%	0.78	0.617 & 0.624	Marcy 1984
1.9	30	0.57	0.623–0.626	Gray 1984
1.9	11	0.21	0.615–0.618	Saar et al. 1986
.....	...	$\leq$0.11[a]	2.208 & 2.227	Saar 1988
3.4	8.4	0.29	0.615–0.618	Saar 1988
2.5	14	0.35	0.563–0.687	Mathys & Solanki 1988
1.0	30	0.30	0.775 & 0.847	Marcy & Basri 1989
1.44.....	8.8	0.13	1.553–1.569	This work

[a] Limit on $|\boldsymbol{B}|f$ is based on Saar's limit of $|\boldsymbol{B}|f^{0.5} \leq 0.4$ kG and an *assumed* field strength 1.5 kG.

Table 6, adapted from Saar (1990), summarizes published magnetic field measurements for ϵ Eri. Both the spectroscopic data and the analysis techniques were quite different in each of these studies. With the exception of one upper limit (Saar 1988), all previous studies have used optical lines and derived higher magnetic fluxes, a significant point which we address below. Using our model of ϵ Eri, we tested whether these previous results are consistent with the observed profile of the $g_{\rm eff}$ = 3 line at 1.56485 μm. We substituted the literature values of $|\boldsymbol{B}|$ and f for our own magnetic parameters and computed model profiles, keeping all other atmospheric parameters fixed. The results are shown in Figure 8 for the four most recent studies. None of the models based on optically determined magnetic parameters is a particularly good fit. The model profiles are typically too shallow in the central part of the profile and too deep at the location of the σ components.

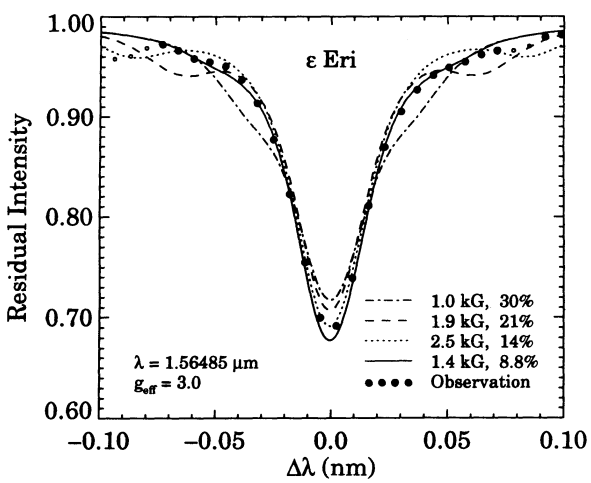

FIG. 8.—Comparison of model line profiles for ϵ Eri, calculated from published magnetic parameters. Our nonmagnetic parameters (see Table 4) were used in all cases. The references can be reconstructed by comparing the plot legend with magnetic parameters in Table 6. The large filling factors deduced in optical studies are all inconsistent with the observed infrared profile, indicated by the filled circles. Unfilled circles indicate blends.

Residuals are shown in Figure 9, which emphasizes the discrepancies in our model of ϵ Eri and three other models from Zeeman analyses of optical lines. The residual profiles show differences between our observed 1.56485 μm line and the model profiles shown in Figure 8. The locus of model points is incrementally displaced by 5% for each model from the literature. The line types match those adopted in Figure 8, and magnetic field properties are listed below each profile. For each residual profile, we calculated χ^2, using only the unblended points (*filled circles*) points. Values of χ^2 in Table 5 refer to a global fit of 16 line profiles, whereas the χ^2 listed in Figure 9 refer only to the 1.56485 μm line. We note that the quality of the fits becomes progressively worse for models with higher surface covering fraction, independent of the field strength. We conclude that the *infrared data rule out covering fractions as high as those found in previous optical studies.*

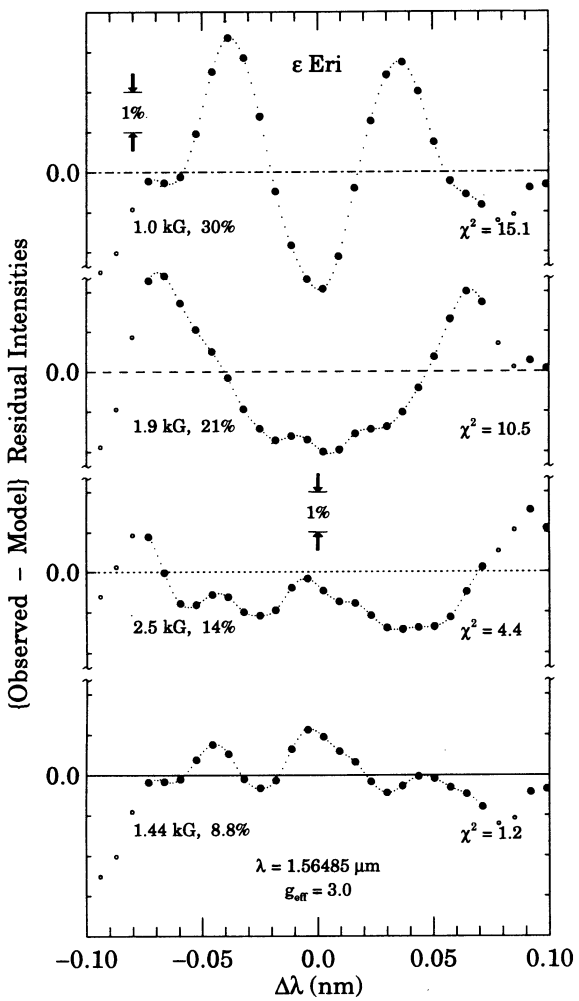

FIG. 9.—Residuals for each of the models presented in Fig. 8. Each model is binned to the observed pixel scale and subtracted from the observed profile. The horizontal lines correspond to perfect fits, with the tick marks along the vertical axis indicating errors of 1% of the continuum. The residual profiles all have the same vertical scale, but successive lines are displaced vertically by 0.05 continuum units. Values of χ^2 are given for each model, based on the unblended points (*filled circles*) in the plot. Models with higher surface covering fractions have progressively poorer fits.

7.2. *Optical and Infrared Dichotomy*

Despite the wide range in individual values of $|\boldsymbol{B}|$ and f in Table 6, Saar (1990) has noted that recent measurements of $|\boldsymbol{B}|f$ using optical lines agree rather well. In light of this, it is particularly striking that our current analysis, which uses higher quality observational data and a more sophisticated modeling procedure, yields a substantially lower value of $|\boldsymbol{B}|f$. In the one previous infrared study of ϵ Eri, however, Saar (1988) saw no evidence for Zeeman broadening in either the Na I line at 2.208 μm or the Ti I line at 2.227 μm. He concluded that fields less than 2 kG had to be confined to less than 5% of the stellar surface, and weaker fields were limited by the observed constraint, $|\boldsymbol{B}|f^{0.5} \leq 0.4$ kG. For an assumed field strength of 1.5 kG, this yields limits on the surface covering fraction and magnetic flux of $f \leq 7\%$ and $|\boldsymbol{B}|f < 0.11$ kG, respectively. Thus, Saar's (1988) infrared Zeeman analysis resulted in magnetic fluxes in agreement with the present study.

Saar's (1988) infrared limit on $|\boldsymbol{B}|f$ contradicts every optical measurement before or since. He concluded that ϵ Eri was in a magnetically dormant state at the time of his infrared observation, but our infrared study also yields very low magnetic fluxes. Moreover, our simultaneous observations of Ca II H and K demonstrate that ϵ Eri was indeed active during the time of our infrared observations (see Fig. 3). Our measured S values of 0.499 and 0.485 for ϵ Eri are only slightly below average (0.510) and well above the minimum recorded value (0.419). The S value of 0.231 for 40 Eri is well above average (0.205) and close to the maximum recorded value (0.252). Mean S values are from Noyes et al. (1984), while extreme S values are from Duncan et al. (1991). We have no simultaneous data for σ Dra, but according to Duncan et al. (1991), the mean S value for this star is 0.218, making it a relatively inactive star.

We also reconstructed the approximate standard deviation of S for all observations between 1967 and 1983 from a table of seasonal standard deviations and number of observations (Duncan et al. 1991). Composite standard deviations for S are 0.018 (ϵ Eri) and 0.006 (40 Eri). Although the S values presumably do not have a Gaussian distribution, these standard deviations do show that ϵ Eri was within its "typical" activity range, whereas 40 Eri was unusually active. On the basis of these S values, we argue that the low values of $|\boldsymbol{B}|f$ deduced in our work on ϵ Eri cannot be attributed to a period of low activity. Nor does it seem likely that all of the optical measurements are spurious. The optical measurements were each based on different data and on quite different methods of determining stellar magnetic properties, and yet they yielded remarkably similar magnetic fluxes.

One difference between optical and infrared diagnostics is their characteristic depth of formation. This leads to differences in $|\boldsymbol{B}|$ and f separately, but their product (magnetic flux) is independent of where in the atmosphere the lines form. Near-infrared lines probe deeper in the photosphere because the continuous opacity contribution of H^- is lower in the infrared. If field strengths are maintained by some sort of equilibrium with the pressure of the surrounding medium, then the field strength will increase with depth. On the other hand, magnetic flux ($|\boldsymbol{B}|f$) must be conserved with depth along vertical flux tubes, so surface covering fraction must decrease with depth to counteract increases in field strength. This gives rise to the common picture of magnetic flux tubes that flare out with height in the photosphere. To avoid the flux conservation requirement, magnetic loops would have to reverse direction in

the photosphere between the depths of formation of the optical and infrared lines. Moreover, to produce larger measured fluxes in the optical, these loops would have to be confined to the upper photosphere. Such structures are not seen in the Sun, nor would they be stable against buoyancy forces. The difference between magnetic fluxes derived in the optical and in the infrared must indicate modeling deficiencies, rather than a real physical effect.

7.3. *Two-Component Analyses*

Some of the discrepancy between magnetic fluxes measured in the optical in the infrared is due to a common assumption that $T(\tau)$ is identical in both the magnetic and nonmagnetic regions. This overly simplistic, but expedient, assumption is not true on the Sun (Schüssler & Solanki 1988), nor do we expect it to hold for other stars. Recent simulations (Basri et al. 1990; Saar & Solanki 1992; Saar, Bünte, & Solanki 1994) have explored, for a few important special cases, how derived magnetic parameters are affected by incorrect assumptions about the atmospheres of stellar magnetic regions. These studies are based on extrapolations of solar flux tube models because very little is known about the structure of stellar magnetic regions. Of the two-component models considered by Basri et al. (1990), model "AK" is probably most relevant to ϵ Eri. For this model, they find that a one-component Zeeman analysis, based on spectral lines at 0.7748 and 0.8468 μm, overestimated $|\boldsymbol{B}|f$ by a factor of 1.33. The "K/K" analysis by Saar & Solanki (1992) is most similar to a single component Zeeman analyses of ϵ Eri. These models predict that $|\boldsymbol{B}|f$ will be overestimated by a factor of 1.17 ($B_U f_U / B_C f_C$ in their Table 1), regardless of whether the line is at 0.6, 1.6, or 2.2 μm. That this error is independent of wavelength is somewhat surprising, given the discussion below. Finally, Saar et al. (1994) consider a one-component Zeeman analysis of a K4 star with two-dimensional flux tubes distributed over the stellar surface. A one-component analysis using the 1.56485 μm line predicts an *underestimate* of $|\boldsymbol{B}|f$ by a factor of 0.93, which has a sense opposite to that predicted by the preceding error analyses. Some of the differences in predicted errors are undoubtedly caused by the wide variety of modeling techniques and spectral diagnostics used in these studies. More research is needed to understand the mechanisms that control errors in derived magnetic parameters.

Some of the basic principles underlying these rather complicated error studies can be illustrated by considering the behavior of a single spectral line that is magnetically sensitive. We compare two models, one with hot magnetic regions and one in which the magnetic regions have the same temperature structure as the quiet atmosphere. Assume the nonmagnetic parameters are already known from an analysis of spectral lines in which the Zeeman effect is weak. The magnetic parameters, $|\boldsymbol{B}|$ and f, are then constrained by the requirement that the sum of quiet and magnetic flux profiles must agree (after continuum normalization) with the observed residual intensity profile. The same constraint must be satisfied, regardless of the temperature structure (hot or quiet) we are using in the magnetic regions. Thus, we can compare magnetic parameters from these two models by noting that the inferred profiles must both match the observed profile and therefore each other. After some algebra, this requirement may be written as

$$\frac{f_{MQ}}{f_{MH}} = \left(\frac{C_{MH}}{C_{MQ}}\right)\left(\frac{R_{MH} - R_Q}{R_{MQ} - R_Q}\right)\left[1 + f_{MH}\left(\frac{C_{MH}}{C_{MQ}} - 1\right)\right]^{-1}, \quad (5)$$

where f is surface covering fraction, C is continuum flux, and R is residual intensity. The subscripts associate each quantity with nonmagnetic regions with a quiet atmospheric structure ("Q"), magnetic regions with a quiet magnetic structure ("MQ"), or magnetic regions with a hot atmospheric structure ("MH"). The MQ quantities are relevant to a one-component Zeeman analysis, whereas the MH quantities would be determined in a two-component Zeeman analysis.

Equation (5) shows how the derived surface filling factor depends on the atmosphere used to describe magnetic regions. The first term in the equation accounts for changes in continuum flux weighting, the second for changes in line depth and shape, while the last is a correction term that is very close to unity. Because the residual intensities vary across the profile, equation (5) cannot be satisfied everywhere in the profile. Particular points in the profile (e.g., line core or center of σ component) may be selected, or more realistically, a least-squares technique may be used to yield a globally optimized solution.

From equation (5), we can see how the surface covering fraction derived in a one-component analysis depends on both the wavelength and the line used in the Zeeman analysis. The term containing the ratio of continuum fluxes arises because a hot magnetic component gets greater weight relative to an MQ model by virtue of a brighter continuum. To compensate for improper weighting, larger surface covering fractions will be inferred in one-component analyses. Moreover, the discrepancy gets larger toward shorter wavelengths because the continuum flux falls off more rapidly in the cool model. To illustrate with an example, in our one-component analysis of ϵ Eri, we deduced a global effective temperature of 5133 K. Stellar magnetic regions were assumed to have the same temperature as quiet regions. Now consider a two-component model in which we use an HM atmospheric model, scaled to an effective temperature of 6000 K, as a crude proxy for a realistic flux tube model. Then the continuum flux at 1.56485 μm in the hot magnetic regions is enhanced by a factor of 1.25 relative to magnetic regions in the one-component model. At 0.8648 and 0.6173 μm, the continuum flux contrasts are 1.63 and 1.88, respectively. Thus, considering only the continuum contrast effect for the moment, we would expect the surface covering fraction derived in a one-component analysis of the 0.6173 μm line to be a factor of 1.5 larger than the same quantity derived using the line at 1.5648 μm. The use of a hot HM model is for illustrative purposes only. More realistic atmospheres having the same effective temperature will give somewhat different enhancement factors.

The other important term in equation (5) is the term involving residual intensities. To help visualize the behavior of this term, we have generated model profiles for the Q, MQ, and MH models for three magnetically sensitive lines that have been used in previous analyses. Profiles for the quiet (*solid line*) and MQ (*dashed line*) components in Figure 10 were generated using our adopted parameters for ϵ Eri. The hot magnetic profiles (dotted line) were generated using an HM model scaled to an effective temperature of 6000 K. Actual flux tube models will yield somewhat different profiles. The abscissa is a velocity, rather than wavelength, scale to facilitate comparison of the optical and infrared lines. The splitting of the σ components is clearly much larger in the infrared line, compared with the optical lines. Now consider the term in equation (5) involving residual intensities. The numerator and denominator are always positive in the line core, and the ratio is greater than 1.

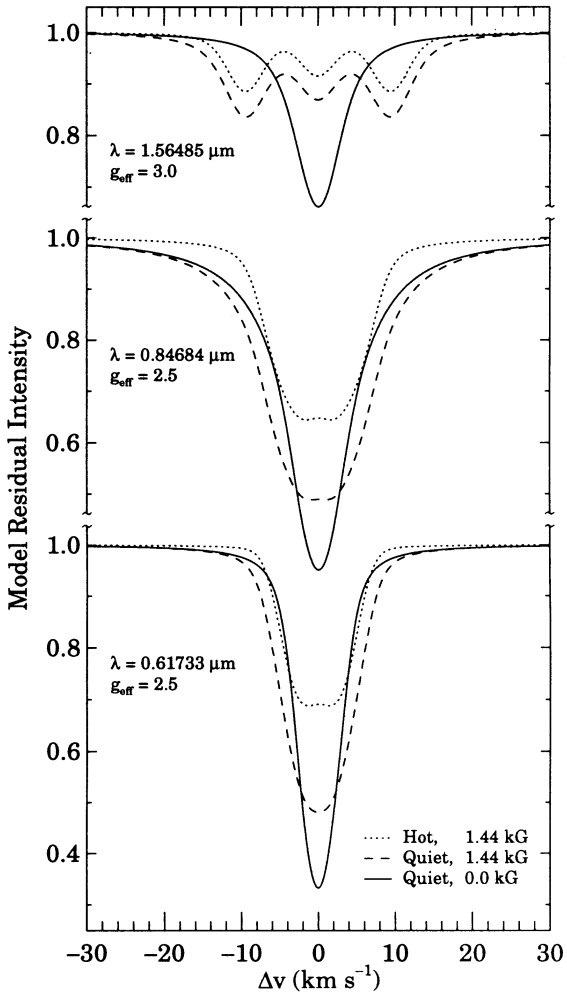

FIG. 10.—Changes in popular magnetic diagnostics as a function of temperature and magnetic field strength. Solid profiles show the residual intensity (R_Q) of the quiet component, as predicted by our adopted model of ϵ Eri (see Table 4). The long-dashed profiles (R_{MQ}) would arise if the quiet atmosphere were threaded with a 1.44 kG magnetic field, whereas the short-dashed profiles (R_{MH}) would arise if the effective temperature of the magnetic regions were 6000 K, instead of 5133 K. The σ components are clearly resolved in the infrared line. All residual intensity profiles have the same vertical scale, but successive lines are displaced vertically by 0.2 continuum units.

This means that to match the line core in a one-component analysis of a two-component star, an erroneously high surface covering fraction is required. The opposite situation occurs in the wings of the infrared line and in most of the wings of the 0.61733 μm line. The numerator and denominator are both negative, and the ratio is less than 1. When these points are considered, the surface covering fraction in a one-component analysis will tend to be less than the actual (two-component) covering fraction. Clearly, both the core and the wings cannot be satisfied.

We recast the constraint that led to equation (5) as a χ^2 minimization problem, and derived an analogous expression for f_{MQ}/f_{MH}. This is closer to the procedure typically used in actual Zeeman analyses but fails to account for changes in nonmagnetic parameters which must occur because the magnetically *insensitive* lines are also affected by the two-component atmosphere. For this reason, we do not present the relation here, but note only that the opposing errors in f_{MQ} due to the core and wings seem to cancel, leaving the continuum contrast effect as the dominant source of error in the derived covering fraction. Finally, we note that the correction term that accounts for changes in residual intensity is actually negative for the wings of the 0.84684 μm line because the profiles from the MH and MQ components straddle the quiet profile. This is unphysical, and in an actual Zeeman analysis the nonmagnetic parameters would have to be changed to compensate.

It has usually been assumed in stellar Zeeman analyses that magnetic signal comes from hotter regions (network and plage), rather than cooler regions (spots), even though both are certainly present. The rationale for this approach is that hotter regions, by virtue of their higher temperatures, will have much brighter continua. The emission from hot regions will dominate spot emission, unless the surface covering fraction of spots greatly exceeds the covering fraction of the hot component. Stellar luminosity and chromospheric emission are correlated on a seasonal timescale for all ordinary cool stars, but anticorrelated on the timescale of a few years for active stars (Radick, Lockwood, & Baliunas 1990). This implies a complicated relationship between spots and hotter active regions in stars such as ϵ Eri. Stellar spots have been inferred from an inverse correlation between TiO band strength and stellar brightness on active stars (Huenemoerder, Ramsey, & Buzasi 1989). Many investigators are pursuing Doppler imaging and Zeeman Doppler imaging of cool stellar features. The existence of cool, annular regions surrounding each flux tube has been postulated on theoretical grounds (Deinzer et al. 1984) or to account for the very low observed continuum contrast seen in most unresolved solar flux tubes (Basri et al. 1990). Grossmann-Doerth et al. (1994) have recently argued that continuum intensity of flux tubes themselves decreases rapidly with increasing flux tube diameter. In light of these results, it may be necessary to include flux tube models with realistic continua or at least a third cool component in stellar Zeeman analyses.

7.4. *The Future*

All the advantages expected of an infrared Zeeman analysis have been realized in this study. Most notably, we have measured the strength of the magnetic field on ϵ Eri with much greater *accuracy* than has heretofore been possible with optical observations. This improved accuracy is possible primarily because the σ components of the $g_{eff} = 3$ line at 1.56485 μm are marginally resolved. The one surprise was our low surface covering fraction, despite a fairly normal level of activity. Higher covering fractions found in optical studies may be due either to temperature contrast effects or to difficulties identifying Zeeman broadening in the optical. The one other infrared analysis of ϵ Eri supports this dichotomy between covering fractions measured in the optical and the infrared. Very high resolution infrared spectrographs, employing fast array detectors, are currently under development. When this equipment becomes available, Zeeman analysis will be much more practical, and the work to understand the role of magnetic fields in controlling stellar activity will begin in earnest.

We are indebted to Ken Hinkle for instructing us in the use of the FTS and reducing the FTS spectra. We also thank Chris Johns for providing the simultaneous optical spectra in support of this project, and Bob Donahue and Sallie Baliunas for providing *S* values in advance of publication. Finally, we thank Sami Solanki, Steve Saar, and Chris Johns for extensive and detailed comments which greatly enhanced the final paper.

REFERENCES

Basri, G., & Marcy, G. W. 1994, ApJ, 431, 844
Basri, G., Marcy, G. W., & Valenti, J. A. 1990, ApJ, 360, 650
Bevington, P. R. 1969, Data Reduction and Error Analysis for the Physical Sciences (New York: McGraw-Hill), 235
Blackwell, D. E., Booth, A. J., & Petford, A. D. 1984, A&A, 132, 236
Deinzer, W., Hensler, G., Schüssler, M., & Weisshaar, E. 1984, A&A, 139, 435
Donahue, R. A., & Baliunas, S. L. 1994, private communication
Drake, J. J., & Smith, G. 1993, ApJ, 412, 797 (DS)
Duncan, D. K., et al. 1991, ApJS, 76, 383
Gray, D. F. 1984, ApJ, 277, 640
———. 1992, The Observation and Analysis of Stellar Photospheres (Cambridge: Cambridge Univ. Press), 409
Gray, D. F., Baliunas, S. L., Lockwood, G. W., & Skiff, B. A. 1992, ApJ, 400, 681
Gray, D. F., & Johanson, H. L. 1991, PASP, 103, 439
Grossman-Doerth, U., Knolker, M., Schüssler, M., & Solanki, S. K. 1994, A&A, 285, 648
Grossmann-Doerth, U., & Solanki, S. K. 1990, A&A, 238, 279
Hall, D. N. B., Ridgway, S., Bell, E. A., & Yarborough, J. M. 1979, Proc. SPIE, 172, 121
Harmanec, P. 1988, Bull. Astron. Inst. Czechoslovakia, 39, 329
Holweger, H., Bard, A., Kock, A., & Kock, M. 1991, A&A, 249, 545
Holweger, H., Heise, C., & Kock, M. 1990, A&A, 232, 510
Holweger, H., & Müller, E. A. 1974, Sol. Phys., 39, 19 (HM)
Huenemoerder, D. P., Ramsey, L. W., & Buzasi, D. L. 1989, AJ, 98, 2264
Jefferies, J., Lites, B. W., & Skumanich, A. 1989, ApJ, 343, 920
Johansson, S., & Learner, R. C. M. 1990, ApJ, 354, 755
Kurucz, R. L., Furenlid, I., Brault, J., & Testerman, L. 1984, Solar Flux Atlas from 296 to 1300 nm (Tucson: NSO)
Landi Degl'Innocenti, E., & Landi Degl'Innocenti, M. 1972, Sol. Phys., 27, 319
Landolfi, M., & Landi Degl'Innocenti, M. 1982, Sol. Phys., 78, 355
Livingston, W., & Wallace, L. 1991, An Atlas of the Solar Spectrum in the Infrared from 1850 cm^{-1} to 9000 cm^{-1} (1.1 to 5.4 μm) (Tucson: NSO)
Marcy, G. W. 1984, ApJ, 276, 286
Marcy, G. W., & Basri, G. 1989, ApJ, 345, 480
Mathys, G. 1990, A&A, 236, 527
Mathys, G., & Solanki, S. K. 1989, A&A, 208, 189
Muglach, K., & Solanki, S. K. 1992, A&A, 263, 301
Noyes, R. W., Hartmann, L. W., Baliunas, S. L., Duncan, D. K., & Vaughan, A. H. 1984, ApJ, 279, 763
Park, J. H., Rothman, L. S., Rinsland, C. P., Pickett, H. M., Richardson, D. J., & Namkung, J. S. 1987, Atlas of Absorption Lines from 0 to 17,900 cm^{-1} (NASA Reference Publication 1188) (Springfield, VA: National Technical Information Service)
Press, W. H., Flannery, B. P., Teukolsky, S. A., & Vetterling, W. T. 1986, Numerical Recipes (Cambridge: Cambridge, Univ. Press), 529
Rabin, D. 1992, ApJ, 391, 832
Radick, R. R., Lockwood, G. W., & Baliunas, S. L. 1990, Science, 247, 39
Rees, D. E., Murphy, G. A., & Durrant, C. J. 1989, ApJ, 339, 1093
Robinson, R. D. 1980, ApJ, 239, 961
Rüedi, I., Solanki, S. K., Livingston, W., & Stenflo, J. O. 1992, A&A, 263, 323
Rüedi, I., Solanki, S. K., Mathys, G., & Saar, S. H. 1994, in Eighth Cambridge Workshop: Cool Stars, Stellar Systems, and the Sun, ed. J.-P. Caillault (ASP Conf. Ser.), in press
Rutten, R. J., & Kostik, R. I. 1982, A&A, 115, 104
Saar, S. H. 1988, ApJ, 324, 441
———. 1990, IAU Symp. 138, Solar Photosphere: Structure, Convection, and Magnetic Fields, ed. J. O. Stenflo (Dordrecht: Kluwer), 427
Saar, S. H., Bünte, M., & Solanki, S. K. 1994 in Eighth Cambridge Workshop: Cool Stars, Stellar Systems, and the Sun, ed. J.-P. Caillault (ASP Conf. Ser.), in press
Saar, S. H., & Linsky, J. L. 1985, ApJ, 299, L47
Saar, S. H., Linsky, J. L., & Duncan, D. K. 1986, in Fourth Cambridge Workshop, Cool Stars, Stellar Systems, and the Sun, ed. M. Zeilik & D. M. Gibson (San Francisco: ASP), 275
Saar, S. H., & Solanki, S. K. 1992, in Seventh Cambridge Workshop: Cool Stars, Stellar Systems, and the Sun, ed. M. S. Giampapa & J. A. Bookbinder (ASP Conf. Ser., 26), 259
Sauval, A. J., Grevesse, N., Brault, J. W., Stokes, G. M., & Zander, R. 1984, ApJ, 282, 330
Schüssler, M., & Solanki, S. K. 1988, A&A, 192, 338
———. 1992, A&A, 264, L13
Solanki, S. K. 1993, Space Sci. Rev., 63, 1
Solanki, S. K., Biémont, E., & Mürset, U. 1990, A&AS, 83, 307
Solanki, S. K., & Brigljević, V. 1992, A&A, 262, L29
Solanki, S. K., Rüedi, I., & Livingston, W. 1992a, A&A, 263, 312
———. 1992b, A&A, 263, 339
Spruit, H. C., & Zweibel, E. G. 1978, Sol. Phys., 62, 15
Steenbock, W. 1983, A&A, 126, 325
Sugar, J., & Corliss, C. 1985, Atomic Energy Levels of the Iron-Period Elements: Potassium through Nickel (New York: AIP)
Unno, W. 1956, PASJ, 8, 108
Unsöld, A. 1955, Physik der Sternatmosphären (Berlin: Springer-Verlag), chap. 82
Valenti, J. A., & Anderson, J. A. 1995, in preparation
Valenti, J. A., Marcy, G. W., & Basri, G. 1994, in Eighth Cambridge Workshop: Cool Stars, Stellar Systems, and the Sun, ed. J.-P. Caillault (ASP Conf. Ser.), in press
Vogt, S. S. 1987, PASP, 99, 1214
Wallace, L., & Livingston, W. 1992, An Atlas of a Dark Sunspot Umbral Spectrum from 1970 cm^{-1} to 8640 cm^{-1} (1.16 to 5.1 μm) (Tucson: NSO)